Effizienzerhöhung für Photonendetektion von mikrostrukturierten Gasdetektoren mittels Materialoptimierung von Konversionsschichten

Masterrarbeit der Fakultät Physik
der
Ludwig-Maximilians-Universität München

vorgelegt von

Nick Andreas Schneider

geboren in Bühl

Betreuer: Prof. Dr. Otmar Biebel

München, den 14.09.2023

Efficiency Increase of Photon Detection of Micro-Structured Gas Detectors via Material Optimisation of Converter Layers

Master thesis of the faculty of physics
at
Ludwig-Maximilians-Universität Munich

submitted by

Nick Andreas Schneider

born in Bühl

Supervisor: Prof. Dr. Otmar Biebel

Munich, the 14.09.2023

Abstract

Micro-Pattern Gaseous Detectors (MPGDs) are heavily used for the detection of charged particles with excellent temporal and spatial resolution. Electrically neutral particles like photons are detected with poor efficiency due to the low density in the active gas volume. By inserting solid converter layers of high-Z material this disadvantage can be mitigated. In this thesis multiple converter layers are placed perpendicular to the amplification region. The converter layers additionally act as the cathode. For amplification a triple GEM foil setup is used. Proper electric fields produced by the converter layers guide the electrons to the amplification region. In order to further increase the photon detection efficiency the material and structure of the converter layers need to be optimised to find the balance between creation and extraction rate. For photon conversion copper plated layers are used with relatively thin FR4 or Kapton as carrier material. In this thesis different converter layer geometries are tested in order to achieve high photon detection efficiencies. These results are compared to simulations for better understanding of the physical processes. The simulations involve Geant4 for particle interaction simulations, ANSYS for calculations of the electric fields and Garfield++ for the simulation of the electron drift. This best performing converter layer type increases the photon detection efficiency by a factor of ≈ 5 compared to the non-optimised layers.

Additionally, environmental effects on the measurements are investigated. Further optimisation possibilities beyond the tested converter layer configurations are discussed using simulations. This improvement provides interdisciplinary possibilities i.e. x-ray imaging in material research, medical physics or astrophysics.

Contents

Chapter 1

Introduction

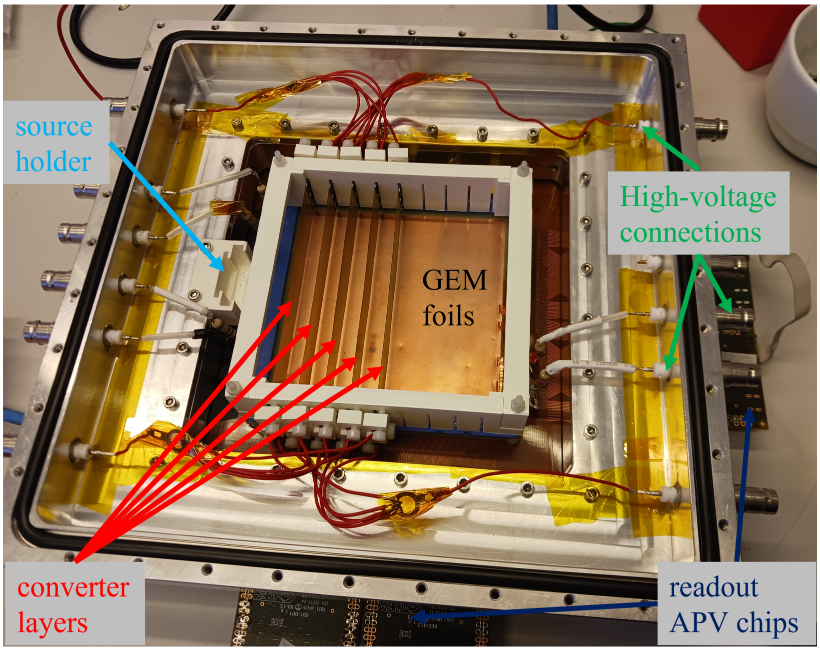

Figure 1.1: Picture of the insides of the detector. Indicated are the converter layers (see chapter 4), the APV chips and the HV connections (see section 3.3), the GEM foils (see section 3.1) and the source holder.

A type of gaseous detectors are Micro-Pattern Gaseous Detector (MPGDs). This type is known for being high rate capable and having a high spatial resolution. Due to their detection medium being gas, which has a naturally low density ρ, they suffer from poor detection efficiency for neutral particles. A better option would be to use semiconductor or scintillator detectors since they have high detection efficiencies for neutral particles due to their high material density. But they are expensive and can not be scaled up easily. On the opposite, gaseous detectors are rather cheap and can be build in up to m^2 dimensions. The low interaction probability in gaseous detectors can be counteracted by inserting solid converter layers which act as a cathode. In this thesis the focus lies on increasing the detection efficiency for photons with an energy of ≈ 60 keV. For this energy the photoelectric effect is the dominant interaction process. Since it's cross section scales with $\sigma_{\mathrm{ph}} \propto Z^5$ the chosen materials for the converter layers are of high significance. Additionally different converter layer geometries are investigated to optimise the thicknesses of the materials. For the measurements performed in this thesis a GEM detector is used (see chapter 3).

The improvement of detection efficiency is useful for x-ray imaging in medical physics reducing the needed radiation exposure of the patient or more generally helpful in detector experiments in high-energy particle physics and nuclear physics.

Chapter 2

Theory

2.1 Particle-Matter-Interaction

Particles can interact via multiple different interaction processes with matter. Some of them result in the production of additional or new particles, which can be used to deduce the incident particle. This will be used in this thesis to detect photons in an ionising gaseous detector by converting them to electrons.

2.1.1 Photons

Since photons are electrically neutral they interact differently with matter than charged particles like electrons, which will be discussed in the next section 2.1.2. Photons mainly interact with electron shell of the atoms by undergoing scattering (Compton effect) or absorption (Photoelectric effect). If the energy of the photon is high enough both cases allow for creation of a primary electron. For even higher energies of at least twice the electron mass the production of an electron-positron pair becomes possible if for example the nucleus is involved to conserve energy and impulse. For the likelihood of these processes refer to figure 2.1. These interaction processes will now be discussed in more detail similar to [1].

The cross sections of these interactions mainly depend on the energy and the material. Due to the purely statistical nature of these effects, photons do not show a definite range in matter. This behaviour is described by the Lambert-Beer law [1]. The exponential attenuation of photons over a distance x follows

$$I(x) = I_0 \cdot e^{-\mu x} \tag{2.1}$$

where I_0 is the incident photon flux and μ is the attenuation coefficient containing the material information. The mass attenuation coefficient is defined as

$$\frac{\mu}{\rho} = \sigma \cdot \frac{N_A}{m_a} \tag{2.2}$$

with the material density ρ, the photon absorption cross section σ, the Avogadro constant N_A and the atomic molar mass m_a. This then leads to figure 2.1.
The radioactive source used in this thesis is made of ^{241}Am emitting 59.54 keV photons [3]. For this energy figure 2.1 shows that the photoelectric effect is dominant. In this case the photon is absorbed and transfers its complete energy to an electron in the atomic shell. If the energy of the photon E_γ is larger than the binding energy E_B of the electron, the electron

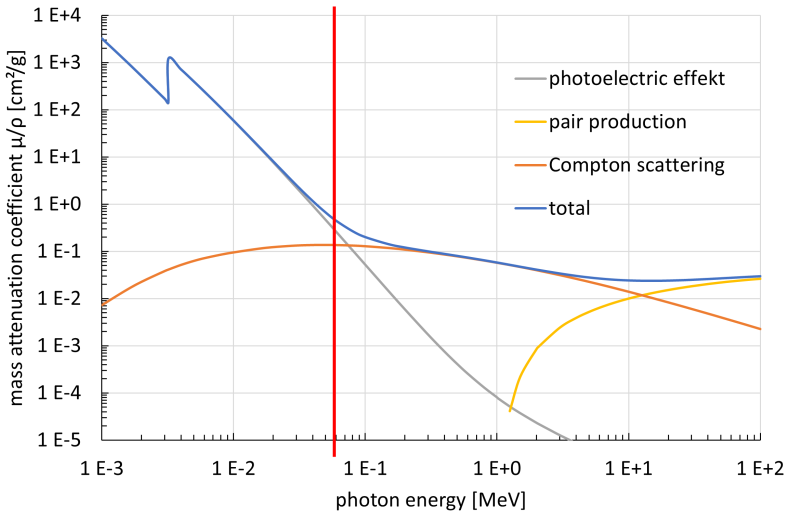

Figure 2.1: The photon mass attenuation coefficient μ/ρ for Ar:CO_2 93:7 % against the incident photon's energy. Three interactions are shown: Photoelectric effect, Compton effect and pair production (Data from [2]). The red line indicates an energy of 59.5 keV.

will escape the atom by ionisation with the energy

$$E_{kin} = E_\gamma - E_B \tag{2.3}$$

The cross section σ_{ph} for non-relativistic particles ($E_\gamma < m_e c^2$) is given by

$$\sigma_{ph} = \frac{32\pi}{3} \cdot \sqrt{2} \cdot Z^5 \cdot \alpha^4 \cdot \epsilon^{-7/2} \cdot r_e^2 \tag{2.4}$$

depending on the atomic number Z, the fine-structure constant α, the reduced photon energy $\epsilon = E_\gamma/(m_e c^2)$ and the classical electron radius r_e [1]. For higher energies Compton scattering is dominant and the energy of the initial photon E_γ gets split up between the outgoing electron energy E_{kin} and the outgoing photon energy E'_γ. If $E_\gamma > 2m_e \approx 1.022$ MeV the photon can create an electron-positron pair with a virtual photon from the nucleus, which is needed for energy and momentum conservation [1]. Of special interest are the photoelectric effect and the Coulomb scattering since they produce an electron-ion pair, which can be detected by the detector.

2.1.2 Electrons

Charged particles like electrons can directly ionise the gas through elastic scattering with an electron in the atom shell. The average energy loss of a heavy charged particle in general per unit length is given by the Beth-Bloch equation [4] with some corrections

$$-\left\langle \frac{dE}{dx} \right\rangle = 4\pi N_{\mathrm{A}} r_e^2 m_e c^2 \rho \frac{Zz^2}{A\beta^2} \left(\frac{1}{2} ln \left[\frac{2m_e c^2 \beta^2 \gamma^2 T_{\max}}{I^2} \right] - \beta^2 - \frac{\delta(\beta\gamma)}{2} - \frac{C}{Z} \right) \tag{2.5}$$

depending on the Avogadro constant N_{A}, the classical particle's radius r_e, the particle's mass m_e, the speed of light c, the density of the material ρ, the atomic number Z, the charge of the particle in units of electron charge z, the atomic mass A, the relativistic velocity of the particle $\beta = v/c$, the Lorentz factor $\gamma = 1/\sqrt{1-\beta^2}$, the maximum energy loss $T_{\max}$, the ionisation potential of the material I, the Fermi density correction factor δ [5] and the shell correction factor C [6]. Since electrons are very light the assumption of them not being deflected as in the case for heavy particles does not hold. Additionally one must consider that the collision happens between two identical particles. Therefore the indistinguishability of the two electrons has to be accounted for. This leads to the following correction of equation 2.5

$$-\left\langle \frac{dE}{dx} \right\rangle = 4\pi N_{\mathrm{A}} r_e^2 m_e c^2 \rho \frac{Z}{A\beta^2} \left(\frac{1}{2} ln \left[\frac{\tau^2(\tau+2)}{2(I/m_e c^2)^2} \right] + F(\tau) - \frac{\delta(\beta\gamma)}{2} - \frac{C}{Z} \right) \tag{2.6}$$

with τ the kinetic energy of the electron in units of $m_e c^2$ and $F(\tau)$ a correction factor considering electron or positron [7].

2.2 Gaseous Detectors Operational Regions

Gaseous detectors generally consist of an anode and a cathode separated by a gas volume producing an electric field. The working principal and working regions are discussed referencing [1]. Incident ionising radiation can interact with the gas or the cathode and produce an electron-ion pair (see section 2.1). This pair is then separated and pulled towards the anode or cathode respectively. In order to obtain significant signals out of the small amount of charge, amplification processes are used. The amplification, further described in section 2.3, mainly depends on the electric field as shown in figure 2.2.

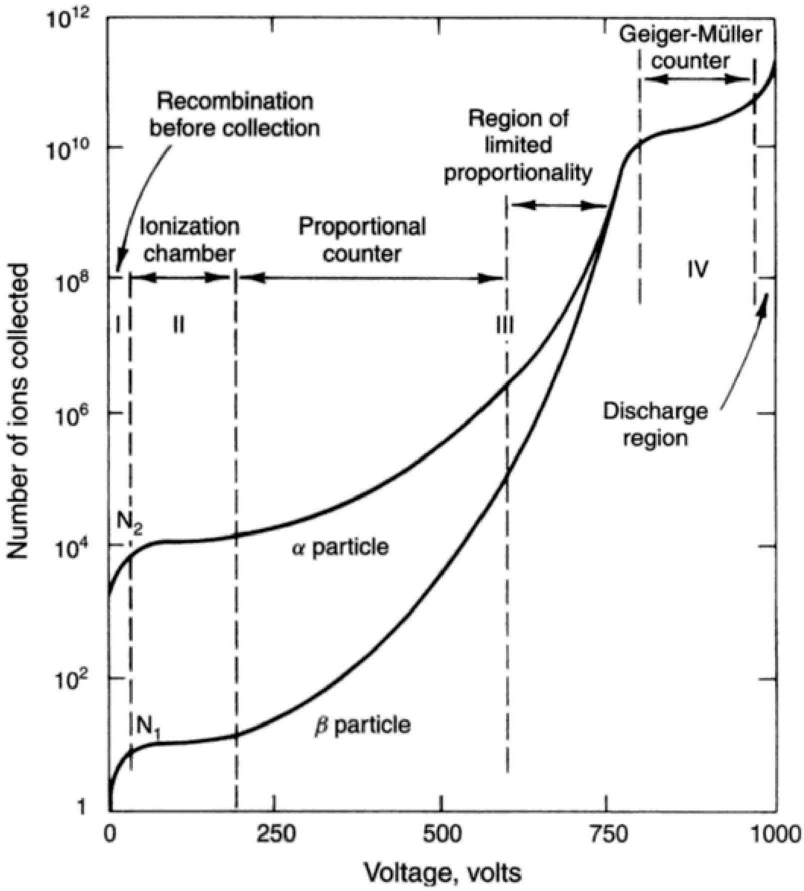

Figure 2.2: Operating regions of gaseous detectors depending on the electric field. Shown are the number of ions collected for α particles and electrons (β particles) as a function of the applied voltage (taken from [8]).

If no voltage is applied (area I in figure 2.2) the electron-ion pairs recombine due to their electric potential. All pairs recombine before they get collected and no signal is detectable.

In the next area the electric field is strong enough to separate the pairs and guide them to the anode/cathode. The current is constant since only few primary electron-ion pairs get produced by the initial source and they do not gather enough energy to further ionise the gas. Therefore ionisation chambers are operated in area II of figure 2.2. If higher voltages are applied the primary electron-ion pair receives enough energy to produce more pairs via ionisation. These then also produce more pairs, creating an avalanche (details in section 2.3). This results in an amplification of the measured signal. The number of additional pairs is directly proportional to the initially produced charge. Detectors in this range are called proportional counters. This direct proportionality comes to an end for higher voltages (see point III in figure 2.2) when the amount of electron-ion pairs is so large that an space charge appears due to the slow movement of the ions compared to the fast drift velocity of the electrons. This weakens the electric field resulting in the electrons gaining less momentum and producing less electron-ion pairs. This limits the proportionality of the amplification in this region. For even higher voltages one reaches area IV in figure 2.2. Here the amount of created electron-ion pairs is so large that a space charge is buildup. This causes the electric field to become weaker resulting in recombination of electrons and ions releasing UV-photons. These photons can produce additional electron-ion pairs in the gas or release an electron from the metal housing of the detector. This leads to the loss of all proportionality. Geiger-Müller counters are operated in this area. Any further increase in voltage leads to random discharges between the anode and the cathode rendering the detector useless [1].

2.3 Gas Amplification

As stated in section 2.2 in proportional counters amplification of the signal is achieved by sufficient electrical fields. At these fields an ionised electron gain enough energy to produce more electron-ion pairs, creating an avalanche. This so called Townsend avalanche [9] is described by

$$\mathrm{d}N = N \cdot \alpha \cdot \mathrm{d}x \tag{2.7}$$

where $\mathrm{d}N$ is the number of new electrons created by N initial electrons travelling over a distance $\mathrm{d}x$ with the first Townsend coefficient α. This coefficient is defined as $\alpha = 1/\lambda = N_\delta \sigma_i$ and describes the probability of ionisation over a path x by inverse mean free path λ. The probability depends on the atom/molecule density N_δ of the gas and the cross section σ_i and therefore α is explicitly dependent on the used gas as well as the pressure p. Rewriting equation 2.7 the total amount of produced electrons is

$$N = N_0 \cdot e^{\alpha x} \tag{2.8}$$

with N_0 primary electrons moving a path x. With this one can define a multiplication factor

$$M = \frac{N}{N_0} = e^{\alpha x} \tag{2.9}$$

Including dependencies of α i.e. the electric field, the gas or the pressure p one gets

$$M = e^{\int_{x_1}^{x_2} \alpha(x) dx} \tag{2.10}$$

for a path between x_1 andx_2. Nowadays the Townsend coefficient gets calculated using computer programs which include dependencies on the used gas or gas mixture, the electric field, the pressure as well as detailed ionisation and excitation processes.

This avalanche effect producing large numbers of electron-ion pairs leads to a drop-like drift behaviour as depicted in figure 2.3. The reason for this is large drift velocity difference of the faster electrons and the slower ions. The multiplication described by equation 2.9 is predicted to grow exponentially but is stopped at the Raether limit of $M < 10^8$ [10]. The slow ions lead to a space charge buildup weakening the electric field. This results in the end of the proportionality region in figure 2.2 described in section 2.2 and limit the gas amplification [7].

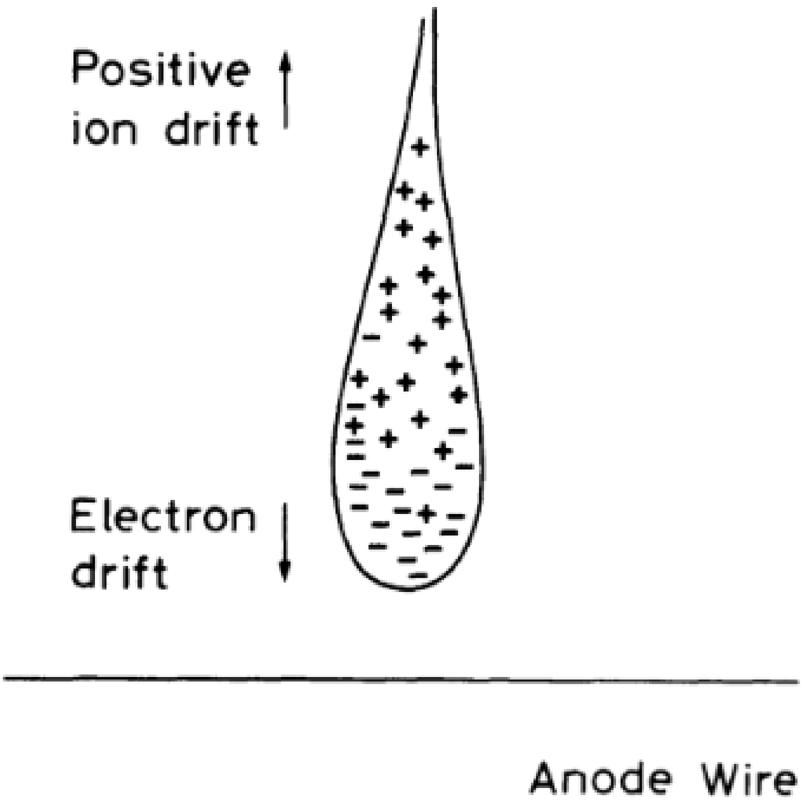

Figure 2.3: Sketch of the drop-like distribution of an electron-ion avalanche drifting towards a thin anode wire. This shape arises out of the higher drift velocity of the electrons forming the bottom of the drop while the slower drifting ions form the tail of the drop (taken from [7]).

Chapter 3

GEM-Detector

In this thesis a GEM (**G**as **E**lectron **M**ultiplier) detector is used and operated as a proportional counter (see section 2.2). It was developed by Fabio Sauli [11] and is a Micro-Pattern Gaseous Detector (MPGD). The GEM detector has the advantages of being high rate capable and having an excellent temporal and spatial resolution.

3.1 Working Principal

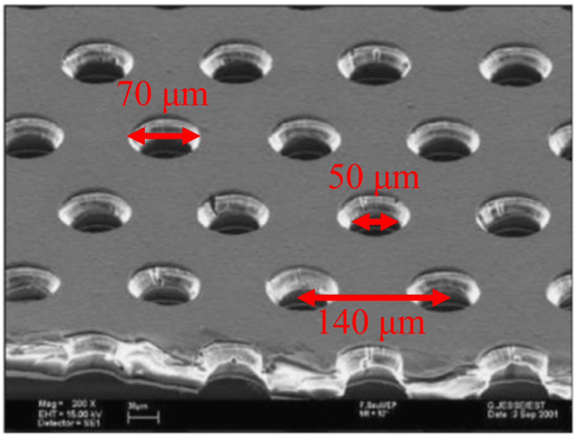

Figure 3.1: Electron microscopic image of a GEM foil showing the hole distribution and structure (adapted from [11])

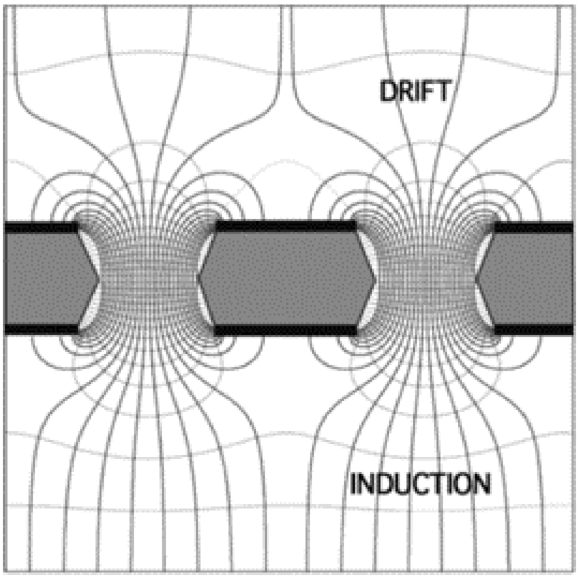

Figure 3.2: Electric field in and around two holes of a GEM foil (taken from [11])

The GEM foil is made of 50 µm thick Kapton foil, which is covered by 5 µm copper on both sides. Using photo-lithography and chemical etching symmetric double-cone-shaped holes are produced with an inner diameter of 50 µm and an outer diameter of 70 µm. There also exist GEM foils with asymmetric holes tapering towards one side. The holes are periodically placed 140 µm apart from each another as shown in figure 3.1. If one applies a voltage difference between the two copper layers, the resulting electric field gets condensed inside the holes leading to locally very strong fields as illustrated in figure 3.2. Typically a difference of about 300 V is applied resulting in an electric field of 60 kV/cm inside the holes. This allows for the creation of electron avalanches (see section 2.3) with a multiplication factor of about $M = 20$ (see equation 2.9). This factor is not sufficient to achieve a measurable signal. That is why one typically uses multiple foils on top of each other (see section 3.2).

3.2 Detector Setup

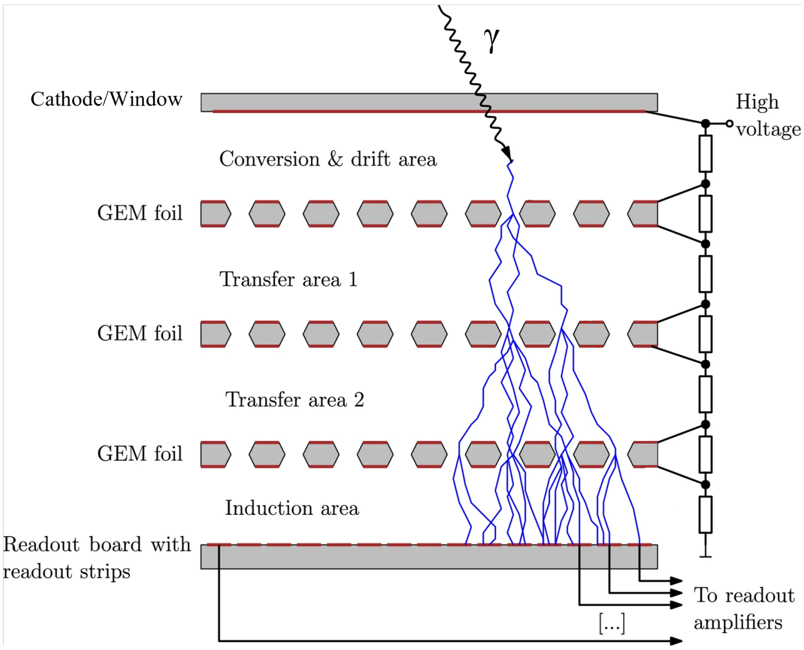

Figure 3.3: Sketch of a triple GEM setup with incident photon producing a signal (adapted from [11])

In this thesis a triple GEM detector is used as sketched in figure 3.3. Three GEM foils result in a total amplification factor of $M = 20^3 = 8000$. If a photon enters the detector through a window made out of aluminium coated Kapton, it might interact with the gas or the cathode and produces at least one electron-ion pair (see section 2.1.1). All electrons are then guided down towards the readout board by the electric fields applied between all components with decreasing negative voltage from top to bottom. The ions are guided upwards to the cathode. Due to differently high converter layers (see section 4.2) two detectors are used one with a drift area of around 2 cm and one with around 10 cm of drift area. The GEM foils are operated with voltage difference of 280 V in order to prevent over-saturation effects in the readout electronics (see section 3.3). If the electrons reach the first GEM foil, they get multiplied in an electron avalanche. The resulting electrons are then guided to the next GEM foil over a gap of 2 mm. The top side and the bottom side of each GEM foil is connected to the high voltage (HV) power source over an 1 MΩ resistor in order to reduce noise and quench discharges. Only the bottom side of the last GEM foil has no resistor since the induced signal of the electrons are used to trigger the readout (see section 3.3). The electrons then drift to the anode and induce a signal. The anode is a PCB (Printed Circuit Board) with two perpendicular layers of 250 copper strips each over an area of $10 \cdot 10$ cm^2. The copper strips have a pitch of 400 µm and a width of 320 µm for the lower layer and a width of 80 µm for the upper layer. These different widths are chosen to ensure a homogeneous charge distribution over both layers. This readout geometry results in a good spatial resolution of less than 100 µm [12].
The casing of the detector is made of aluminium in order to act as a Faraday cage, reducing noise sources. It has multiple gas tight HV connections for the GEM foils and the cathode.

In this thesis the cathode is replaced by converter layer (see chapter 4).
There are two gas connections to continuously flush the detector with Ar:CO_2 in a ration of 93:7 vol.%. Argon is used as main detector gas for gas amplification and CO_2 quenches UV photons getting emitted during amplification. A slight over-pressure of 1-5 mbar is achieved with a bubbler (end of pipe a few cm deep in water) at the end of the gas line. This over-pressure is needed to prevent oxygen, water vapour and other contaminants leaking into the detector. The detector is placed in a climatised cabinet to hold the temperature at $25 \pm 0.3°$ and the relative humidity at $25 \pm 3\%$. This stabilises the operating conditions. A picture of the detector setup is visible in figure 3.4.

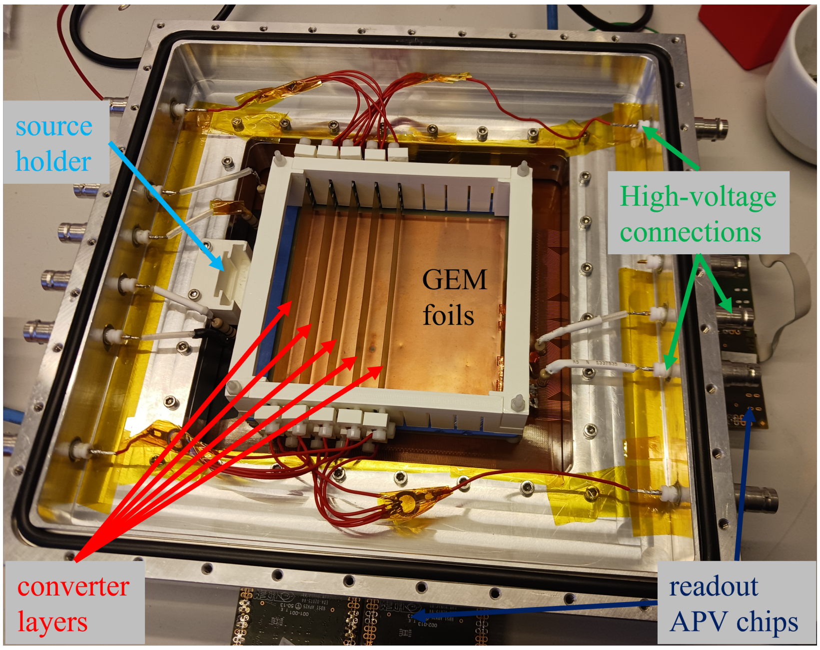

Figure 3.4: Picture of the insides of the detector. Indicated are the converter layers (see chapter 4), the APV chips and the HV connections (see section 3.3), the GEM foils (see section 3.1) and the source holder.

3.3 Readout Electronics

Figure 3.5 shows the connection scheme of the readout electronics and the HV power supply. All GEM foil sides and the cathode are connected independently and the voltages are regulated remotely by a computer. Only the bottom side of the lowest GEM foil is connected to a preamplifier in order use the induced signal of the electrons, passing the last GEM foil, as a trigger signal. This signal is increased by the preamplifier and then distributed by a linear fan-in/fan-out (Fi/Fo) device. Its main purpose is to feed the signals after all individual steps to an oscilloscope for visualisation. The signal then gets shaped by the Timing Filter Amplifier including smoothing and adjusting to a Gaussian shape. The Discriminator sends a rectangular signal pulse if the incoming signal exceeds a previously set threshold. Getting the pulse from the Discriminator, the Dual Timer adapts the signal length and sends it to the Front-End Concentrator (FEC) card [14]. The FEC uses this signal as a trigger signal to start the readout of the detector. The signal of the anode is collected by APV25 front-end boards [15], which have 128 channels each. Two APVs (one master, one slave) are needed for each readout plane since there are 250 strips per plane. The Analogue-Digital-Converter (ADC) converts the analogue APV signal to be read by the FEC-card. Over an Ethernet

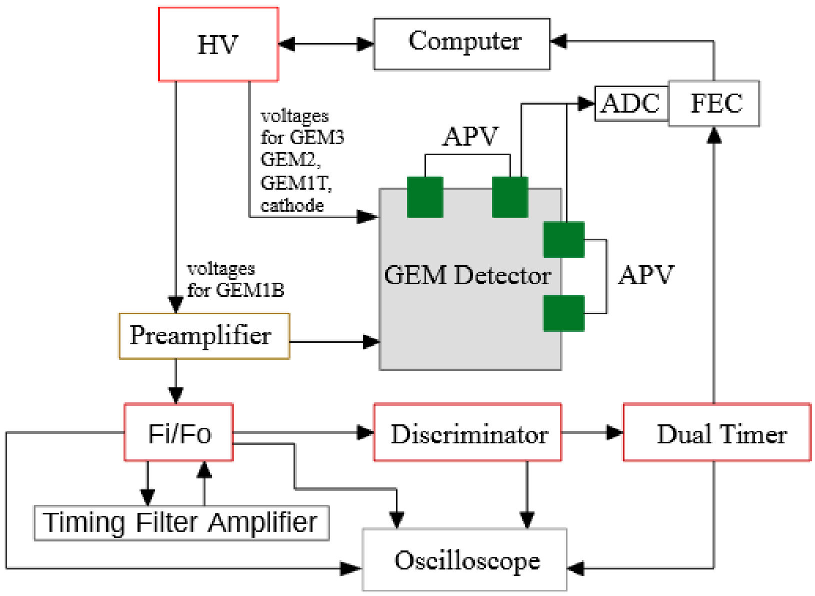

Figure 3.5: Scheme of readout electronics and high voltage (HV) supply. For GEM1 "T" stands for the top side and "B" for the bottom side (from [13]).

cable the data is send to a Data Acquisition (DAQ) computer with a specific software (see section 3.4) recording it. The computer can be used to vary the applied voltages even while taking data. With this setup a time-resolved single strip readout is achievable.

3.4 Software

The data send by the FEC is collected by mmDAQ (micromegas DAQ) [16]. One of the features is an online background suppression by loading in a pedestal run taken with a random trigger. Information such as charge per strip and timing are saved in a root-file [17]. This root-file is the post-processed and analysed by a software written by Bernhard Flierl [12]. An exemplary signal is shown in figure 3.6. The signal rise is fitted to an inverse Fermi function described by

$$q(t) = \frac{Q}{1 + e^{\frac{t-t_0}{\sigma}}} + q_0 \tag{3.1}$$

with the charge distribution maximum Q, the point of inflection t_0, a rise time measure σ and the baseline offset q_0 [12]. The main parameters by which the signal gets characterised are the maximum charge Q and σ. In order to suppress noise, only signals with $\sigma > 3$ ns or $Q > 500$ a.u. are counted. All other signals get rejected and ignored. Due to the amplification process, lateral diffusion or charge sharing between strips nearly all signals are induced in more than one strip. Therefore clustering is applied and adjacent hits get combined. The resulting cluster is described by its charge

$$Q_{\text{cluster}} = \sum_{\text{strips}} q_{\text{strip}} \tag{3.2}$$

and by its position

$$x_{\text{cen}} = \frac{\sum_{\text{strips}} x_{\text{strip}} \cdot q_{\text{strip}}}{Q_{\text{cluster}}} \tag{3.3}$$

This way of determining the cluster position is called the centroid method. The hit position is reconstructed out of the charge weighted strip position over the total cluster charge Q_{cluster}.

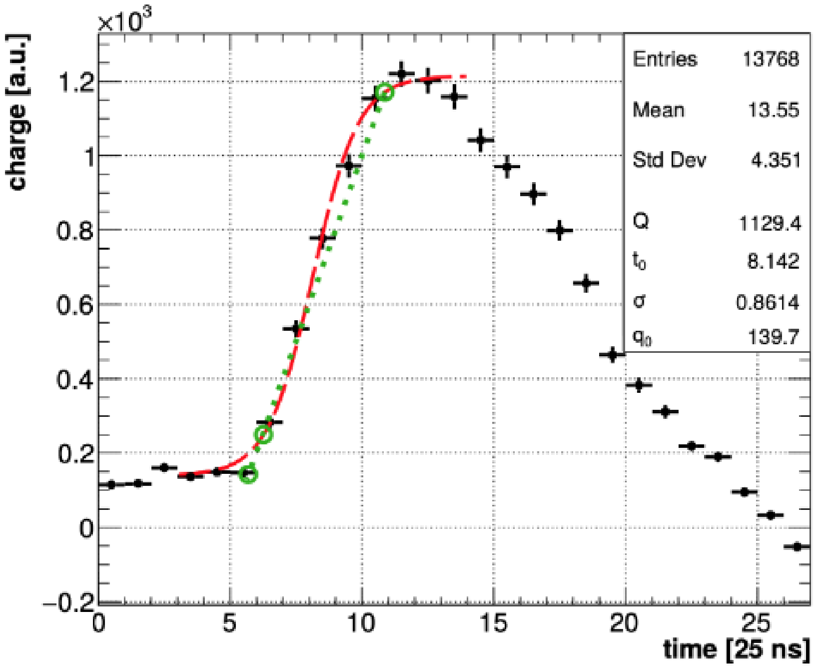

Figure 3.6: Exemplary signal from a single strip fitted with a Fermi function (red curve) (taken from [12])

This is combined to the charge weighted mean hit position (see 3.3) and is used for further investigations.

Chapter 4

Efficiency Increase of Photon Detection using Conversion Layers

Gaseous detectors suffer from poor detection efficiencies for neutral particles due the naturally low density of gases. The idea is to insert solid converter layers and thereby improve the detection of photons. Additionally, these converter layers can act as a cathode and produce an electric guiding field for the electrons (see section 5.1.2).

4.1 Theoretical Principle

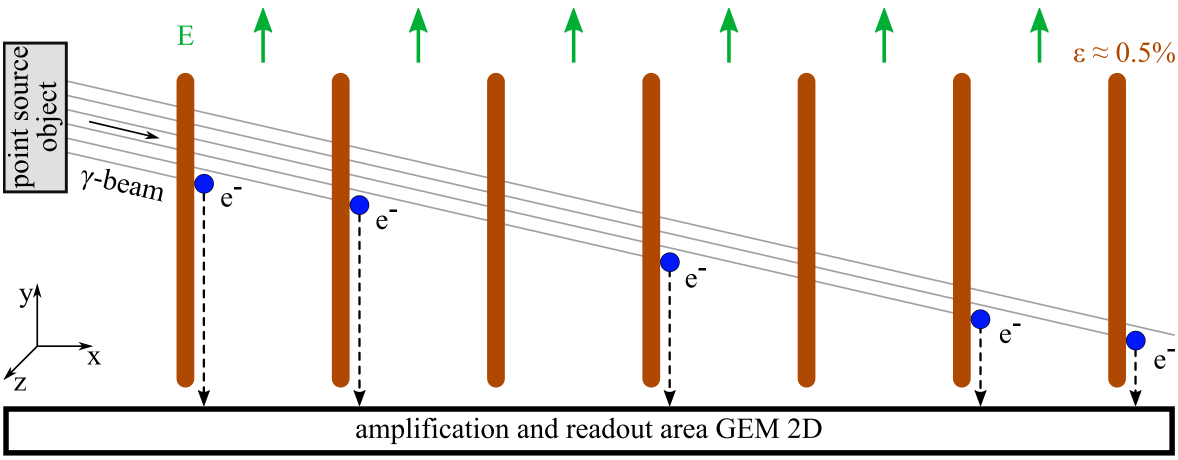

Figure 4.1: Sketch of conversion layers increasing the interaction probability of photons by $\approx 0.5\%$ per layer. The resulting electrons get guided to the amplification and readout layer (from [18])

For 59.5 keV photons figure 2.1 shows that the photoelectric effect is dominant in Ar:CO_2 93:7 %. Due to the strong dependency of the photoelectric effect on the atomic number $\sigma_{\mathrm{ph}} \sim Z^5$ (see equation 2.4), the photoelectric effect becomes even more dominant for high Z materials. Since the converter layers should also act as the cathode, an good electrical conductor is needed. Copper is a good candidate as it has a relatively high $Z = 29$ and is an excellent conductor. Silver or Gold would possibly be even better, but are not used because of their cost. A 35 µm thick layer of copper has a conversion probability of $\approx 0.5\%$ at 59.5 keV photon energy [19]. In order to use the converter layers as a cathode, the copper cannot cover the hole area but has to be subdivided. To keep up the stability the copper is put on a substrate. But this substrate is also absorbing photons and acts as passive material. Figure 4.1 illustrates to basic idea of this setup. To find the optimal thicknesses of the copper and the substrate is a major point in this thesis.

4.2 Converter Layers

4.2.1 General Layout

A converter layer consists of a non-conductive substrate with copper strips on either side to act as the converter and to produce the electric guiding field. Multiple different layers were produced by a external company. All investigated layers have the same general structure, but vary from the others in the parameters. There are a five parameters in total: the width of the copper strips w, the distance between two copper strips d, the thickness of the copper strips x_{Cu}, the thickness of the substrate x_{sub} and the total number of the copper strips $\#_{\mathrm{Strips}}$, which is set to always be 25. For further illustration of the parameters see figure 4.2.

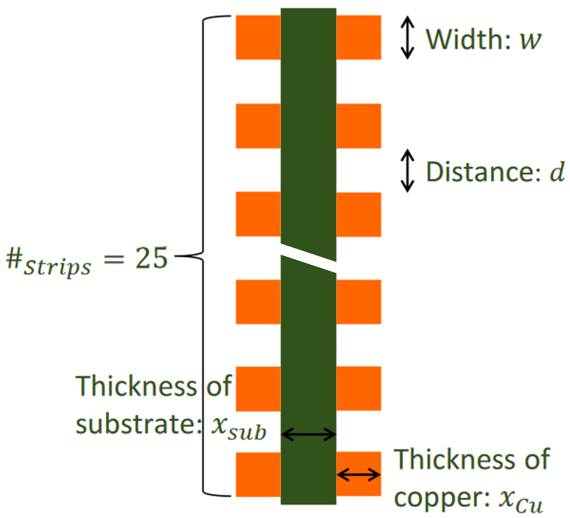

Figure 4.2: Schematic sketch of the profile of a converter layer with relevant parameters

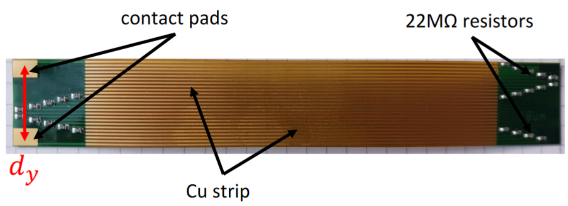

Figure 4.3: Picture of a converter layer with annotations

Figure 4.3 shows the side view of one converter layer. The copper strips are clearly visible in the middle part and cover an area of $20 \cdot 100$ mm^2. To both sides the substrate is visible. On the substrate 22 MΩ SMD-resistors are soldered on in order to connect the 25 copper strips and produce a voltage gradient over the layer. On the left the contact pads for the HV connection can be seen. The voltage difference applied to these contact pads is called d_y. What effect d_y has on the measurements can be seen in figure 6.9. Nearly all converter layers have total height of $h_L = 20.6$ mm and a total length of $l_L = 135$ mm. The specific characteristics of all used layers are covered in section 4.2.2.

4.2.2 Specific Layouts

In the following all investigated layers will be discussed in detail. Only the parameters that deviate from the standard values are mentioned. The standard values are: total number of strips $\#_{\mathrm{Strips}} = 25$, total layer height $h_L = 20.6$ mm, total layer length $l_L = 135$ mm, strip width $w = 0.4$ mm and strip distance $d = 0.4$ mm. The reason for the chosen thicknesses and materials are that they are commercially available and therefore rather cheap and consistent in quality. For further explanation of the naming scheme used to describe the different conversion layer types see figure 4.4.

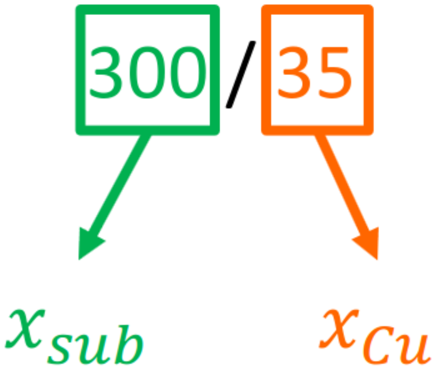

Figure 4.4: Illustration of the naming scheme describing the different conversion layer types. The first number in front of "/" is the the thickness of the substrate in µm. The second number corresponds to the copper thickness in µm. **Note**: The substrate material is not explicitly specified, but implicitly referred to since there are no layers of different substrate material with the same x_{sub} due to material limitations.

1550/35

Figure 4.5: Picture of 1550/35 conversion layer made of FR4. 300/35 layers look almost the same.

The layer shown in figure 4.5 is made of FR4, which is a fire-retardant version of G10, a standard PCB material with 7-8% bromide. It has x_{sub} = 1550 µm and x_{Cu} = 35 µm. It does not bend or curve at all.

300/35

This layer is thinner than the layer shown in figure 4.5 but looks the same. It is also made of FR4, but has x_{sub} = 300 µm and x_{Cu} = 35 µm. It is slightly flexible and permanent deformations are easy to correct.

100/35

This layer's substrate is made of a Kapton-like polyimide (from now on just called Kapton). It has x_{sub} = 100 µm and x_{Cu} = 35 µm. This version is flexible and it mainly deforms elastically, such that it bends back or only little pressure is needed to correct deformations. It looks nearly identical to the layer visible in figure 4.6.

100/18

Figure 4.6 shows this layer. As with 100/35 layer, the substrate is made of Kapton. It's parameters are $x_{\mathrm{sub}} = 100$ µm and $x_{\mathrm{Cu}} = 18$ µm. Therefore it has less copper than all previous layers. It is slightly more flexible than 100/35 and sightly easier deforms inelastically.

Figure 4.6: Picture of 100/18 conversion layer made of Kapton-like polyimide. 100/35, 50/35 and 50/18 look very similar.

50/35

This layer has $x_{\mathrm{sub}} = 50$ µm and $x_{\mathrm{Cu}} = 35$ µm. Because of the Kapton being this thin, the layer is floppy and is deformed easily. It is nearly impossible to get rid of all deformations. It looks basically alike the one shown in figure 4.6.

50/18

This is the thinnest of all investigated layers with parameters of $x_{\mathrm{sub}} = 50$ µm and $x_{\mathrm{Cu}} = 18$ µm. It is therefore also the floppiest and easiest to deform. Once deformed it is as hard to bend back as 50/35.

Large Layers

These layers are called large layers because it's copper strips have a width of $w = 3.6$ mm and the standard distance of $d = 0.4$ mm. In order to maintain the number of strips $\#_{\mathrm{Strips}} = 25$ the total height of the layer had to become $h_L = 100$ mm. Considering the other parameters it has the same thicknesses as 50/18, but proves to be way more rigid because of the larger amount of copper. The copper makes also more difficult to get rid of deformations. A picture of a large layer can be seen in figure 4.7.

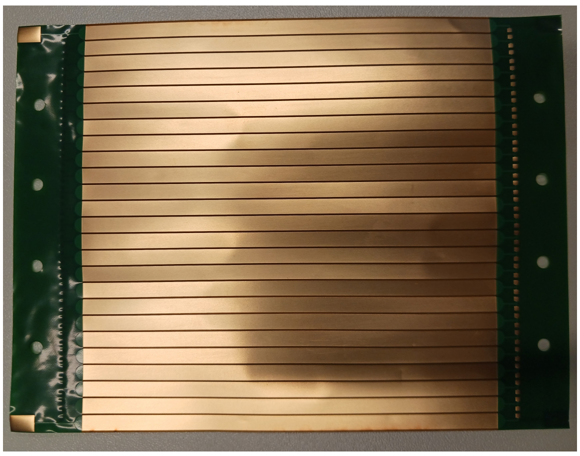

Figure 4.7: Picture of a large conversion layer

Even thinner layers with $x_{\text{sub}} = 25$ µm where produced but turned out to be very hard to work with. Soldering the resistors on the layers would strongly deform the layers due to the heat and the solder joints were very unstable and unreliable. This rendered these layers useless and they were not investigated.

4.3 Support Structure

Due to flexibility of all of the layers produced with Kapton as the substrate material (see section 4.2.2) a special support structure is needed. This support structure is able to put stress on the layers by pulling them straight. This minimises any deformations already in the layers and prevents the layers to move or bend when the detector is carried after assembly. This support structure can be seen in the detector in figure 3.4 or seen closeup in figure 4.8. For further details see appendix A. For the large layers an adapted version is made.

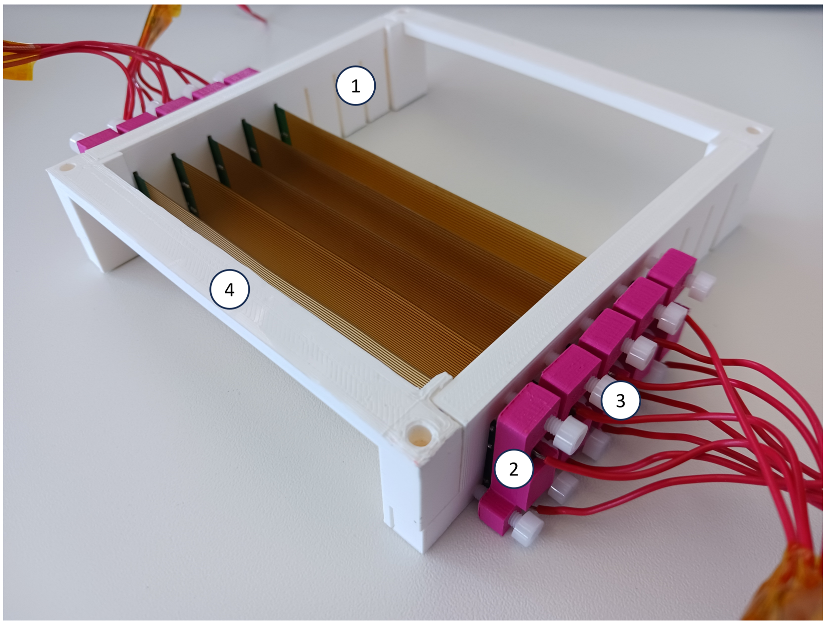

Figure 4.8: Closeup picture of the support structure holding the converter layers in place. Four main components are visible: (1) the white main structure (see figure A.1) holding the layers upright and in place, (2) the pinkish structures (see A.2) at the ends of each layer held in place by a screw jamming the layer in between itself and the structure, (3) the screws applying stress to the layer when screwed in and pushing against the main structure, (4) the stabilisation arms (see figure A.3) between the main structures preventing them to tilt under the applied forces.

Chapter 5

Simulation

In order to predict and better understand measurement results simulations are performed. To get a good representation of the involved physical processes multiple specialised software packages are used: Geant4, ANSYS and Garfield++. The results of these simulations are then compared to the measurements.

5.1 Software Packages

5.1.1 Geant4

Geant4 (**GE**ometry **AN**d **T**racking) simulates the particle-matter interactions in the detector. It is a specialised tool-kit developed at CERN (see [20]). It covers all conversion and ionisation processes happening in the detector and simulates the trajectory of all primary and secondary electrons (see chapter 2). The simulation is given a to scale model of the detector components including the material compositions. Unfortunately, the exact composition of the FR4 and Kapton-like polyimide are unknown since they are company secrets. The support structure made of PLA (polyamide) is neglected because not being in the sensitive volume and the interaction probability of 59.5 keV with the plastic is small. The GEM foils and the detector housing are simplified since no amplification is simulated and the source is positioned inside the detector. The source is emitting mono-energetically 59.5 keV photons in 4π. The momentum, energy and position of the electrons can be written out and saved at any time. Figure 5.1 shows the irradiated model.

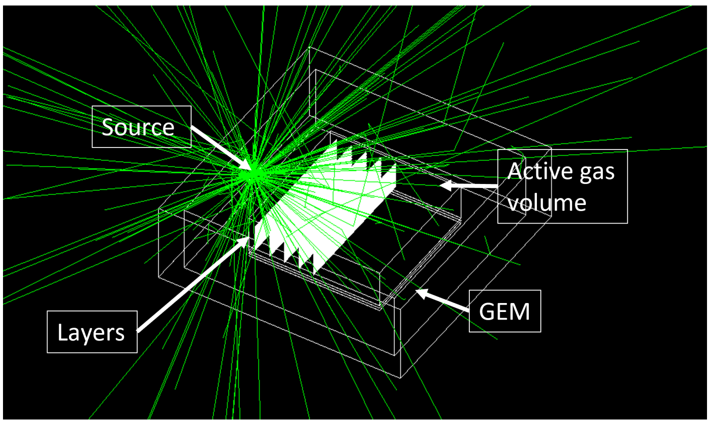

Figure 5.1: Illustration of a few events in Geant4. Visible is the detector setup with the relevant components, mainly the converter layers. The green lines are the photon trajectories.

5.1.2 ANSYS

ANSYS (**AN**alysis **SYS**tem) is a finite-element analysis software (see [21]). It can be used for a variety of simulations, but in this thesis it is used to simulate the electric field inside the detector. To achieve that a three-dimensional model of the detector is created and voltage constraints are applied to the converter layer strips and the anode. The resulting electric field and geometry is exported to be used by Garfield++.

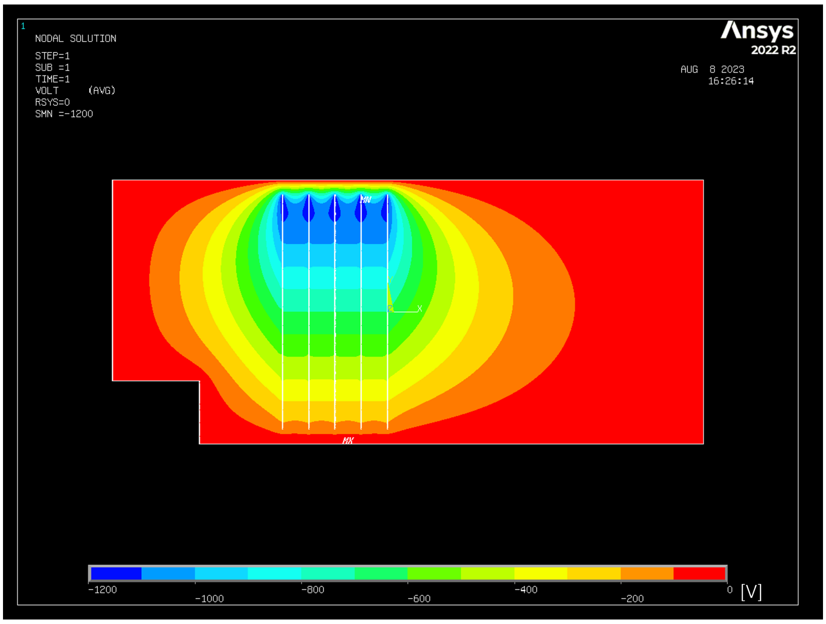

Figure 5.2: Electric field simulation of ANSYS with the housing and the anode set to ground. Between the top and the bottom of the converter layers a voltage difference of 1000 V is set. The colours indicate the equipotential lines of the field. An electron would move perpendicular to them.

5.1.3 Garfield++

Garfield++ (see [22]) is a software tool-kit specialised for gaseous detectors. It's main purpose in this thesis is the simulation of the electron drift. It is given the electron's position, momentum and energy information simulated by Geant4 (see section 5.1.1) and the electric field map calculated by ANSYS (see section 5.1.2). Garfield++ is capable of simulating the ionisation process, but is only used here for the electron drift. For this it uses the MAGBOLTZ simulation package (see [23]). MAGBOLTZ has access to a large database with the properties of the involved material on which the drift depends such as energy loss, excitation levels, cross section, density and more. With this information it is able to calculate the drift velocity, the Townsend coefficient (see section 2.3) and the diffusion and thereby solve the Boltzmann transport equations.

5.2 Simulation Design

In the following some general results are discussed. For comparisons between simulation and measurement see chapter 6 or 7.

5.2.1 Electron Production Distribution

A basic plot to check if the simulation is working as intended is the production distribution of electrons shown in figure 5.3. In this figure all electron's production positions are marked if they at some point reach the active gas volume above the readout area (see section 3.2). Electrons that get produced but do not reach the active gas volume are not counted. One can clearly see the radially decreasing distribution due to the source emitting in 4π. The total number of photons simulated is 10 million with ≈ 2.7 million reaching the active gas volume. Comparing the 2D-distribution with the 1D-distribution of the production of primaries in copper in figure 5.4, one would expect to see the converter layers in the 2D-distribution, but they are not visible. This indicates although production in copper being high, only very few reach the gas. This is further discussed in section 5.2.2.

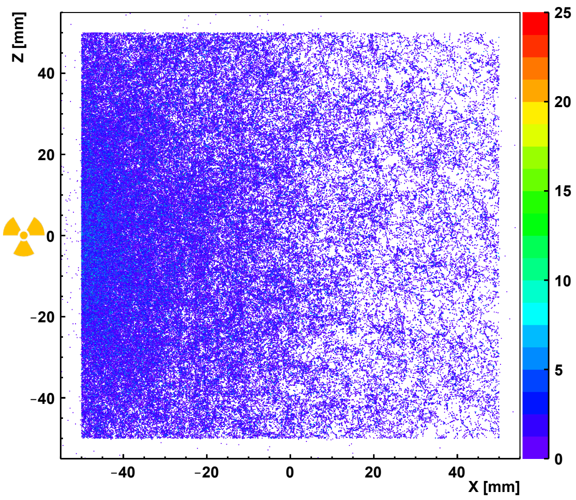

Figure 5.3: Production XZ-position of all electrons that reach the active gas volume in a Geant4 simulation. The source is positioned at $(X, Z) = (-78.25, 0)$ [mm] indicated by the radioactive symbol. A clear radial distribution is visible. Simulated with 50/18 layers.

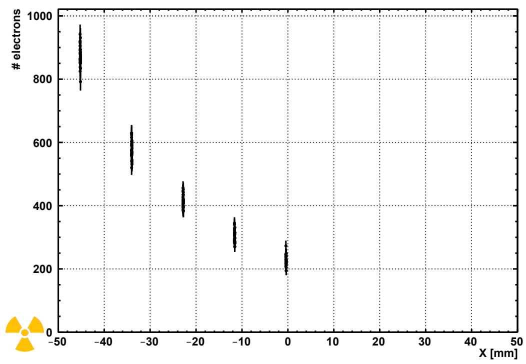

Figure 5.4: Production of primary electrons in Cu against X-coordinate. The source is positioned at $X = -78.25$ mm indicated by the radioactive symbol. Simulated for 50/18 layers. An exponential decrease can be observed.

The energy distributions of all electrons that reach the active gas volume is shown in figure 5.5. There is an increase in number from low energies to higher energies ending in a broad peak at ≈ 40 keV followed by a dominant peak at ≈ 50 keV. After this peak the number of electrons falls off immediately with a small plateau at high energies. The reason for this can be seen in figure 5.6.

In figure 5.6 the energy distribution of primary electrons getting created in different materials in the detector are shown. The Compton-edge for all materials can be seen at ≈ 10 keV. The most primary electrons get produced in the copper which shows a broad peak at ≈ 40 keV and a very sharp and high peak at ≈ 50 keV. This very high peak originates from the k-shell electrons of the copper being ionised and having to overcome the binding energy of 8.979 keV (from [24]), as described by equation 2.3. This then results in the peak at ≈ 50 keV in figure 5.5. Note that the peak height difference between the sharp and the broad peak in figure 5.5 is a factor of ≈ 2, while in figure 5.6 it is a factor of ≈ 125. This leads to the assumption that the structure of figure 5.5 is strongly dominated by these k-shell electrons scattering and therefore losing energy before they escape from the copper to the gas. That

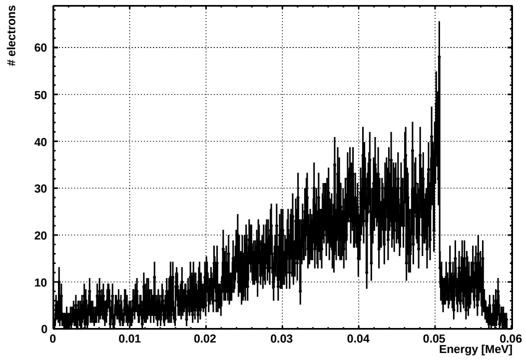

Figure 5.5: Energy distribution of all electrons as they reach the active gas volume. Simulated for 50/18 layers. A broad, wide peak and a sharp peak can be seen.

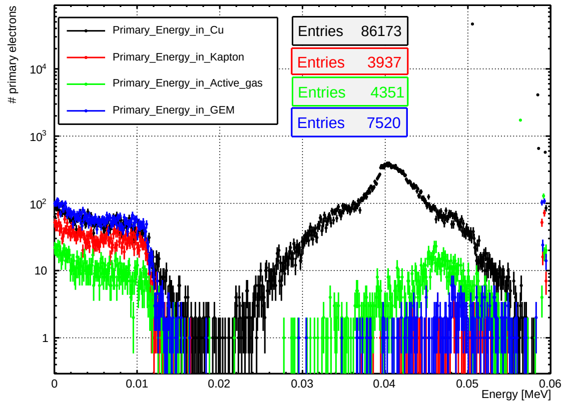

Figure 5.6: Energy distribution of primary electrons at production in copper (black), Kapton (red), the active gas volume (green) and the GEM foil (blue). Simulated for 50/18 layers. The Compton edge and photoelectric effect peak are visible.

the broad peak in figure 5.5 is not caused by secondary electrons exiting the copper can be seen by the fact that 2234 primary electrons produced in copper reach the gas while only 31 secondary electrons reach the gas. In consequence the broad peak in figure 5.5 corresponds to the broad copper peak in figure 5.6.

5.2.2 Electron Production and Extraction Efficiency

As realised in section 5.2.1 the amount of electrons produced in the copper strips of the converter layers (see figure 5.4) is not reflected in the 2D-distribution of all electrons reaching the active gas volume (see figure 5.3). To investigate this effect a simplified simulation is performed with a planar source with 59.5 keV irradiating a slab of copper in front of a gas volume. In front of the copper a block of FR4 is simulated. For a sketch of this setup see 5.7. The thickness of the copper is varied. The results are shown in figure 5.8. This figure shows the conversion rate of photons into electrons and the extraction rate of electrons into the gas volume against the thickness of the copper. While the production rises exponentially, the extraction first rises exponentially but then saturates at ≈ 5 µm. This effect is further illustrated by figure 5.9. It depicts the creation of electrons in copper and the extraction of electrons into the gas dependent on the x-coordinate. It can be seen that only electrons extract if they are less than 5 µm away from the copper surface. In this 5 µm range the amount of extracted electrons decreases exponentially and even within 1 µm of the surface only $\approx 60\%$ of the created electrons extract. The CSDA-range (Continuous Slowing Down Approximation) for 50 keV electrons in copper is ≈ 7.7 µm [25] which is slightly more than what is predicted by the simulation. The reasons for this discrepancy may be unknown surface effects that need additional energy to be overcome. Consequently, no electrons that are produced in the FR4 manage to penetrate the copper and reach the gas.
This leads to the conclusion that all copper thicker than 5 µm acts only as passive absorber material. This causes total production efficiency to be small. The total production efficiency is calculated by dividing the number of events with any electron reaching the active gas

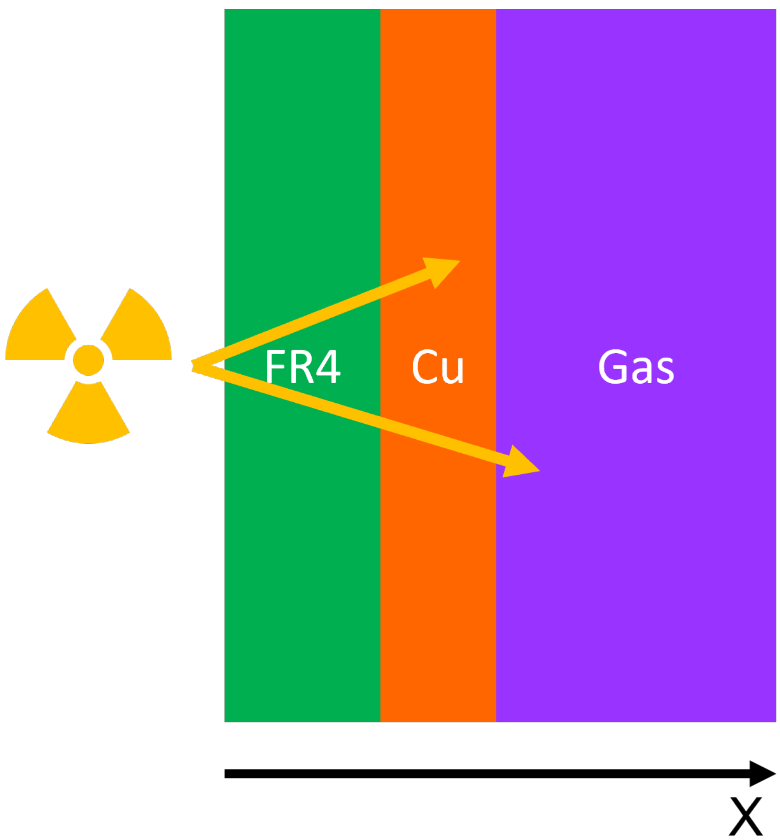

Figure 5.7: Sketch of the simple simulation setup to investigate the electron extraction probability. It consists of the source irradiation a slab of FR4 followed by a copper plane of variable thickness and after that a gas volume is positioned.

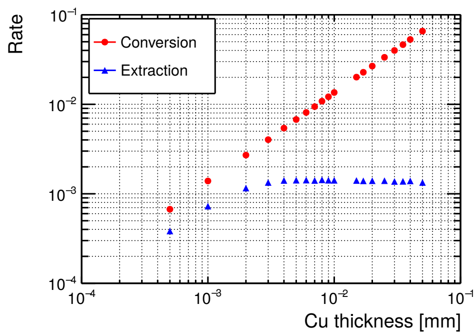

Figure 5.8: Conversion rate and extraction rate against the thickness of copper (from [18]). While the conversion rises the extraction saturates.

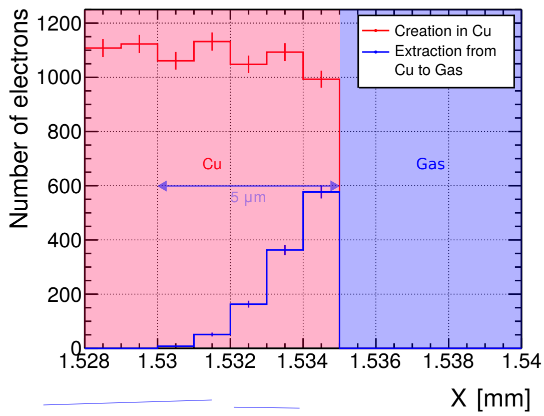

Figure 5.9: Number of created electrons and number of extracted electrons in the surface region between copper and gas (from [18]). The amount of extracted electrons decreases exponentially with the distance to the surface.

region by the number of events with the initial photon passing the active gas volume. For the 50/18 converter layers from which simulation results where shown in section 5.2.1 the total production efficiency is $\approx 0.87\%$.

5.2.3 Electron Guiding Fields and Efficiency

In order to simulate the guiding behaviour of the converter layers first the electric field is calculated by ANSYS (see section 5.1.2) using a voltage difference of $d_y = 600$ V (see figure 4.3). Some resulting plots can be seen in figures 5.10 and 5.11.

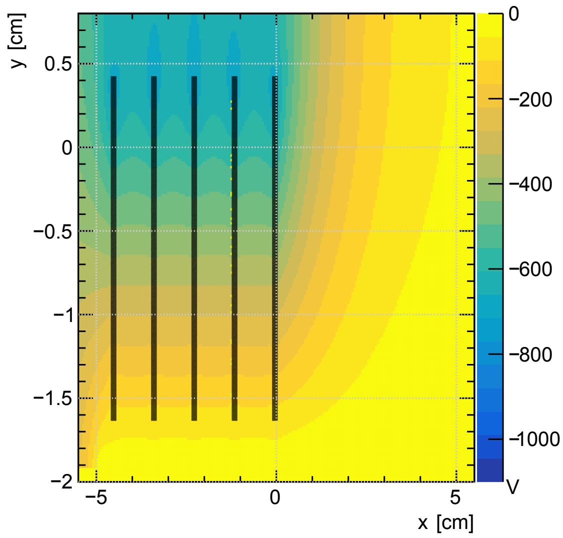

Figure 5.10: Potential field corresponding to the equipotential lines of the electric field. An electron moves perpendicular to these lines from negative to positive voltage. Simulated with 1550/35 layers and $d_y = 600$ V (from [18]).

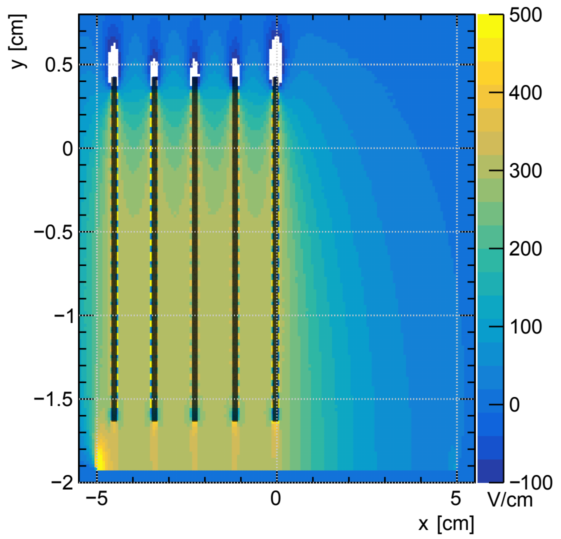

Figure 5.11: Electric field strength in V/cm. The strongest field is in the lower half of the converter layers except for boundary effects directly below the layers. The field at $x > 0$ decreases with distance to the last layer. Simulated with 1550/35 layers and $d_y = 600$ V (from [18]).

In figure 5.10 the potential distribution is depicted. The lines between the colour gradient correspond to the equipotential lines of the electric field, thus an electron moves perpendicular to them. In the lower half of the layers the equipotential lines are in parallel which means that electrons get guided straight down. There is a little bit of displacement happening in the upper part because of the lines being bulged out a bit. All electrons getting produced at $x > 0$ will get dispersed over a large area due to the equipotential lines fanning out towards the right side. As shown in figure 5.11 the electric field is mainly focused between and under the layers and is only weak above and to the sides of the layers. Directly above and below the individual layers boundary effects can be seen, due to last copper strips having the same potential applied and the field lines adapting to that. At the lower half of the layers the electric field is relatively constant. Above the layers the electrons move slowly in between the layers as seen by the low electric field strengths visible in figure 5.11 and the equipotential lines in figure 5.10. To understand how different converter layers change the guiding distribution one looks at the electric fields produced by them under different circumstances. Figure 5.12 shows the equipotential lines of the electric field of 50/18 layers with a drift voltage of $d_y = 600$ V. The equipotential lines are nearly in parallel in the lower half of the layers but strongly fan out to the right side past the layers. Compared to figure 5.10 the boundary effects at the end of the layers are weak. The field in the upper half is more homogeneous for 1550/35 than for 50/18. All in all the electric fields of the different converter layers are very similar.

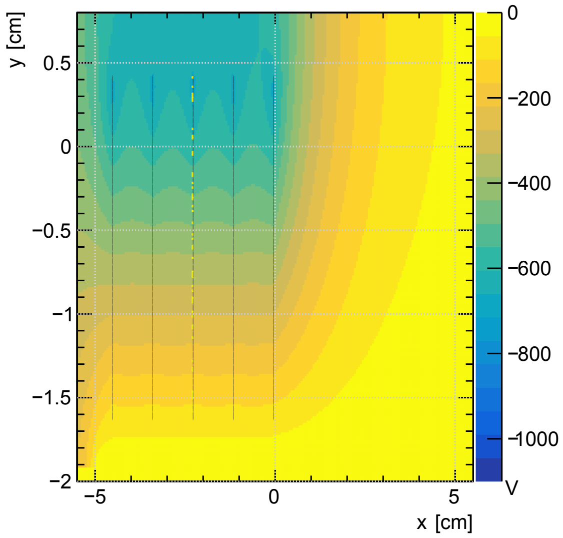

Figure 5.12: Potential field corresponding to the equipotential lines of the electric field for 50/18 layers and $d_y = 600$ V. An electron moves perpendicular to these lines (from [18]).

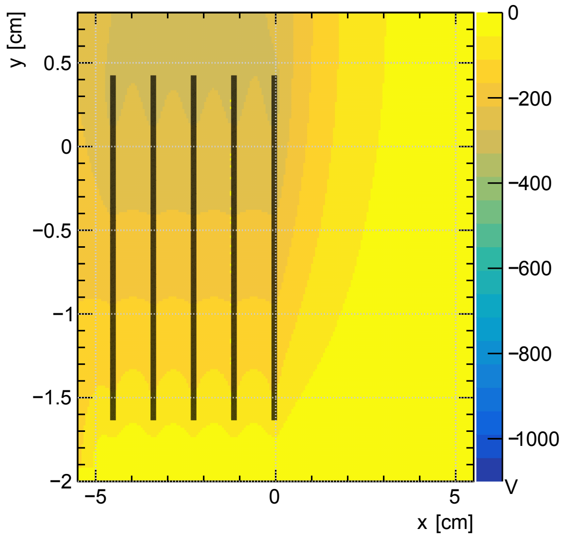

Figure 5.13: Potential field corresponding to the equipotential lines of the electric field for 1550/35 layers and $d_y = 200$ V. An electron moves perpendicular to these lines (from [18]).

Figure 5.13 compared with figure 5.10 shows the effect of the drift voltage on the electric field. There is no electric field for $d_y = 0$ V. That is the reason why figure 5.13 shows the case of $d_y = 200$ V. The electric field in between the layers is not homogeneous and the low density of equipotential lines show that the electric field is weak as expected for only $d_y = 200$ V. The field to the right of the layers does not reach that far out compared to figure 5.10. While the boundary effects in figure 5.10 are mainly on the top sides of the layers, figure 5.13 has relatively strong boundary effects at the bottom sides of the layers. The conclusion is that the most homogeneous electric field is achieved by the thinnest converter layers with the highest drift voltage d_y.

5.2.4 Electron Spatial Distribution

Considering the drift behaviour explained in section 5.2.2 on can understand figure 5.15 which is the result of combining the electric field of figure 5.10 from ANSYS with the starting positions of the electrons depicted in figure 5.14 simulated by Geant4 (see section 5.1.1). These information are given to Garfield++ (see section 5.1.3), which simulates the drift of the electrons. In order to be counted as detected an electron needs to pass the lower limit of $y = -1.9$ cm. In this Garfield++ simulation recombination effects are not considered because of the range of an electron in the used gas mixture (Ar:CO_2 93:7 vol.%) which mainly consists of Argon, a noble gas, for which recombination or electron attachment is very unlikely. The guiding efficiency can be calculated by comparing the amount of entries in both figures 5.14 and 5.15. In this case 46780 out of 80834 electrons are detected resulting in an guiding efficiency of $\approx 52\%$. There are multiple reasons for an electrons not reaching $y = -1.9$ cm: the electron gets guided outside the simulated volume (mainly to the left and right), the electron stops moving by hitting the converter layers or the drift time of the

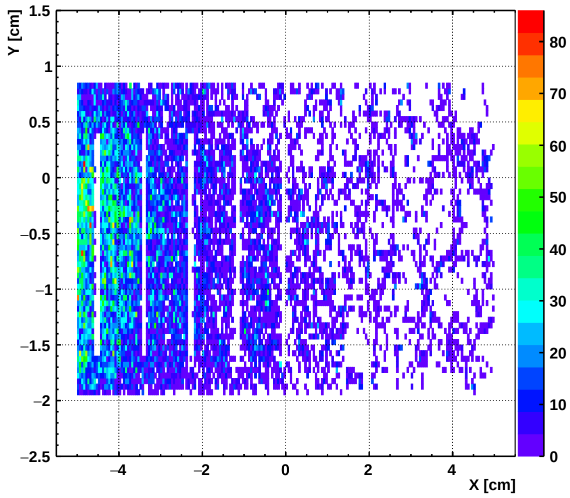

Figure 5.14: Starting positions of the electrons determined by a Geant4 simulation used as input for the Garfield++ simulation resulting in figure 5.15 (from [18]). One sees the radial distribution due to the point source and the positions of the 1550/35 converter layers.

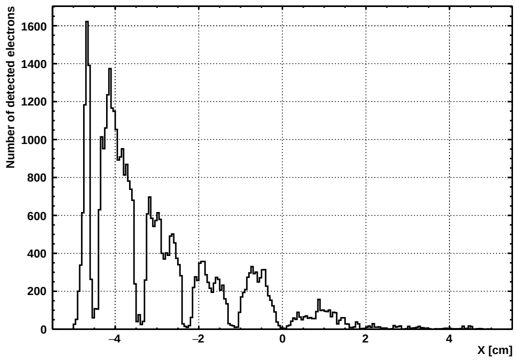

Figure 5.15: End position in x-direction after successful drift. Simulated for 1550/35 layers, d_y = 600 V and a time-cut of 800 ns (from [18]). An exponential decrease with minima corresponding to the converter layer positions is visible.

electrons exceeds the applied time-cut. Here the time-cut, set at 800 ns, is applied after all electrons where simulated. A time-cut is used to mimic the finite time of data taking in the real detector due to memory limits of the readout electronics and to get rid of the perfect simulation conditions. An electron exceeding the time-cut would not be accounted to the correct event. The time-cut is chosen by comparing figure 5.16 with actual measurements. The chosen value reflects the real trigger rate to d_y behaviour. The trigger rate shown in figure 5.16 is calculated by equation 5.1

$$f = \rho_{\text{prod}} \cdot \rho_{\text{extr}} \cdot A \tag{5.1}$$

multiplying the simulated production and guiding efficiencies ρ_{prod} and ρ_{extr} of events with the activity A of the real source.

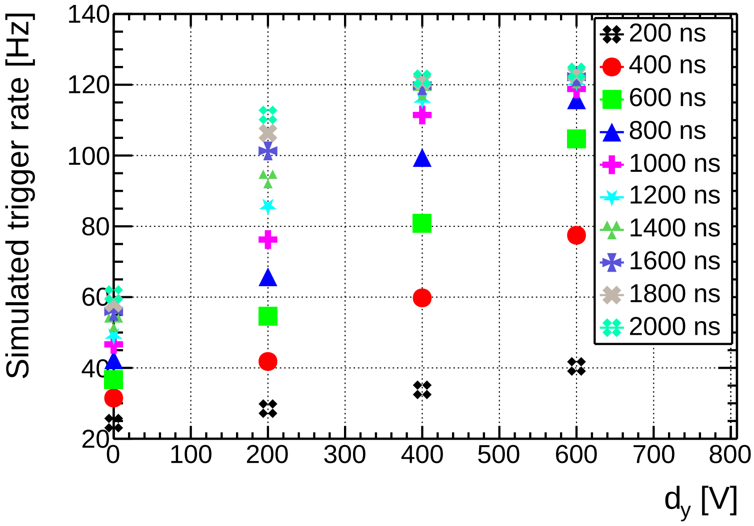

Figure 5.16: Simulated trigger rate against drift voltage d_y for different time-cuts. Short time-cuts result in linear behaviour while long time-cuts show saturation (from [18]).

Chapter 6

Investigation of Small Layers

In this chapter all converter layers except the large layer are measured and compared to simulation. First the measurement results are discussed and different layer types get compared. Then simulation results comparing the layer types are introduced and later compared with the measurements.

6.1 Measurement

The measurements are done with the setup described in section 3.2 and with the readout explained in sections 3.3 and 3.4.

6.1.1 Hit Distribution

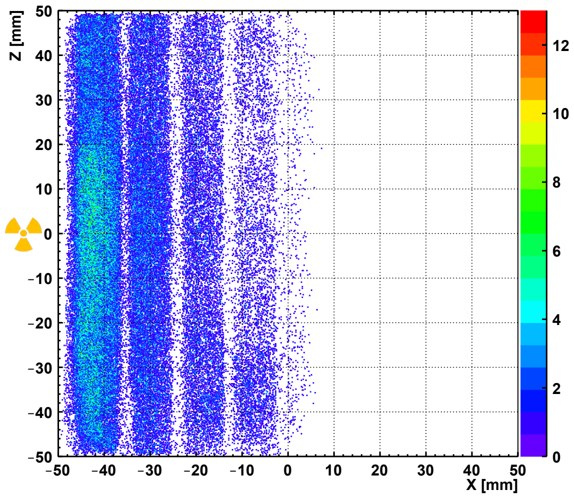

Figure 6.1: Measured exemplary 2D hit distribution with $d_y = 600$ V. The source is positioned at $(X, Z) = (-78.25, 0)$ [mm] indicated by the radioactive symbol. The minima corresponding to the layer positions can be seen clearly.

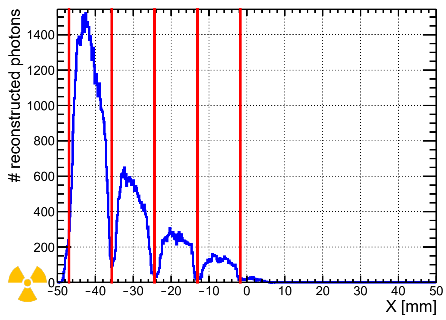

Figure 6.2: Profile in X-direction from figure 6.1 with $d_y = 600$ V. The red boxes indicate the layer position and thicknesses. The source is positioned at $X = -78.25$ mm indicated by the radioactive symbol. There is an $1/r^2$ decrease for rising values of X.

Figures 6.1 and 6.2 show the results of a measurement with 100/18 layers and $d_y = 600$V. The 2D hit reconstruction distribution shows 5 distinct areas corresponding to the areas between the converter layers. The density of hits is the highest in the first area since the source is placed at $(X, Z) = (-78.25, 0)$ [mm] and thereby the first layer covers the largest angle relative to the source. The subsequent areas cover smaller angles and photons might be already absorbed in previous layers. The last area has only very few and scattered hits. The positions of the layers become even more visible when looking at figure 6.2. It shows the x-profile of the measurement in figure 6.1. 5 minima can be seen, each corresponding to one layer. The position and thickness of the layers are indicated by the red boxes. They match with the minima. There is an $1/r^2$ decrease visible caused by the shrinking angle coverage and the absorption happening in the gas and the previous layers. The region in front of the first layer and behind the last layer only have very few reconstructed photons. The reason for this will be discussed in section 6.3.
The difference in the x-profiles for all converter layers can be seen in figure 6.3. The measurements of all but 50/18 have a very similar event count. It shows that the minima become thinner for thinner layers and that the maxima get slightly broader. The curve for 50/18 is higher than the rest due to it having a longer measurement time and therefore recording more events. The red curve corresponding to 300/35 is shifted to the right for $x < -25$ mm because of to much pressure on the GEM foils which is then slightly bend upwards, resulting in an artificial displacement of electrons towards the middle of the detector. That might also be the reason why only 100/35 shows a very small peak at $x \approx -48$ mm. The other measurements depicted here possibly experienced a GEM foil bending strong enough to push this very first peak into the first major peak but weak enough to not displace the whole structure. The peak with a width of one bin at $x = 0$ mm mainly seen for 50/18 is a result of the first APV chip (see section 3.3) ending and the next one beginning. Therefore it is readout artefact and has no physical meaning.

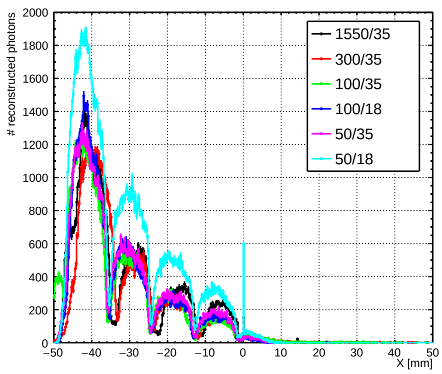

Figure 6.3: Profile in X-direction for different layer types at drift voltage $d_y = 600$V. The line for 50/18 is shifted because of it's event count being larger. For all curves an $1/r^2$ decrease is visible.

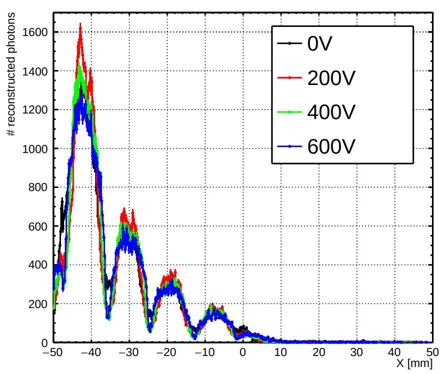

Figure 6.4: Profile in X-direction for different drift voltages d_y and with 100/35 layers. All curves show an $1/r^2$ decrease.

In figure 6.4 the x-profile of the hit reconstruction for different drift voltages d_y is depicted. With smaller $d_y \neq 0$ V the peaks get sharper and higher because of the drift field getting less homogeneous (see figure 5.12). Therefore the electrons get pushed to the middle between the converter layers. At $d_y = 0$ V the electrons reach the readout only due to the electric field of the GEM foils, the field between the bottom side of the layers and the upper most GEM foil and diffusion in the gas. That is the reason why the detector still sees events although not having a drift field. For higher d_y the minima become more narrow and more dominant since they are now dominated by the layer thickness. The electric field guides the electrons nearly perpendicularly towards the readout. The very first small peak is separated stronger from the first major peak with rising d_y and the last peak at $x > 0$ mm becomes broader because the electric field reaches further away from the last layer for higher d_y.

6.1.2 Cluster Charge

The cluster charge describes the charge distribution of all clusters (see section 3.4). The amount of clusters per event can be seen in figure 6.5. Since the number of clusters per event

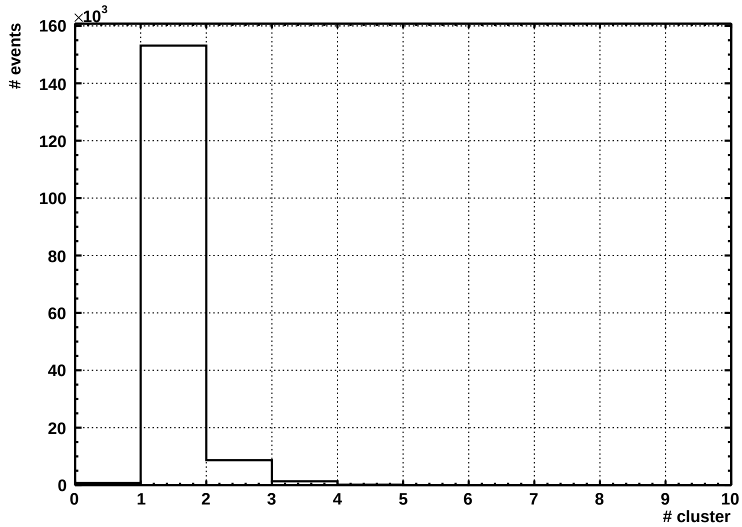

Figure 6.5: Number of clusters per event for 50/18 converter layers. For nearly all events only one cluster is measured.

is nearly always one, the cluster charge represents the total collected charge quite well. Due to the analogue charge signal getting converted to a digital signal, the charge is given in channels of the Analogue Digital Converter (adc channels). The total height of the cluster charge just represents the charge collected during measurement and therefore is directly dependent on the measuring time since the source is always the same. Figures 6.6 and 6.7 show the cluster charge spectrum for different converter layers and for different drift voltages d_y respectively.

All converter layers made out of Kapton (100/35, 100/18, 50/35, 50/18) show a similar structure in figure 6.6. They have a dominant high peak about 3000 adc channels and a second broad peak at around 5000 adc channels. The layers with 50 µm of substrate have a higher second peak compared to the first peak than the 100 µm thick layers. The second peak 100/35 lies more to the right than the others at about 5500. 300/35 has the second peak even higher than the first one while 1550/35 only has one very broad peak. Both layers made of FR4 (1550/35, 300/35) have their first peaks more to the right than the layers made of Kapton.

The first high peak should be due to the source emitting 59.5 keV photons which predominantly produce 50 keV electrons in the copper. As shown in figure 5.5 there are also electrons with smaller energies. Now two effects become important: The $\propto 1/\beta^2$ behaviour of the Bethe-Bloch equation for electrons (see equation 2.6) at these low energies and the finite travel length of the electrons due to the converter layer distance of ≈ 1 cm. In combination these effects cause lower energetic electrons to deposit more energy before they reach the next

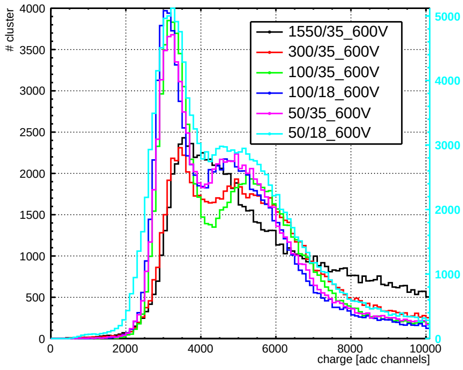

Figure 6.6: Cluster charge for the different converter layer types with $d_y = 600$ V. 50/18 is scaled to become comparable to the others. Most curves show a double-peak structure.

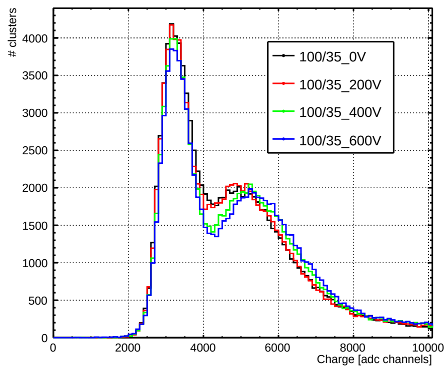

Figure 6.7: Cluster charge for 100/35 converter layer with multiple drift voltages d_y. The double-peak structure varies slightly between the curves.

layer as the higher energetic electrons. This leads to the detector measuring more charge for lower energy electrons. This is further explained in table 6.1.

initial energy [keV]	collision loss $[\frac{\text{MeV}\cdot\text{cm}^2}{\text{g}}]$	ρ_{Ar} $[\frac{\text{g}}{\text{cm}^3}]$	total loss $[\frac{\text{keV}}{\text{cm}}]$
10	14.97	1.66E-3	10 (24.85)
12.5	12.70	1.66E-3	12.5 (21.10)
15	11.10	1.66E-3	15 (18.43)
17.5	9.907	1.66E-3	16.45
20	8.974	1.66E-3	14.90
25	7.610	1.66E-3	12.63
30	6.657	1.66E-3	11.05
35	5.950	1.66E-3	9.877
40	5.404	1.66E-3	8.971
45	4.969	1.66E-3	8.249
50	4.613	1.66E-3	7.658
55	4.317	1.66E-3	7.166

Table 6.1: Energy deposit of electrons with different initial energies in Ar over a distance of 1 cm (Data from [25]). Lower energy electrons deposit more energy in the detector before hitting the next converter layer limited by the initial energy.

Therefore, the second peak is caused by lower energetic electrons predicted by figure 5.5. This double peak structure does not change drastically when altering the drift voltage d_y as can be seen in figure 6.7. It further shows that the first peak becomes slightly smaller with increasing d_y while the second peak moves to higher charges. With the second peak moving, the minima between the peaks is more dominant at high d_y. The peak structure is not changing strongly under variations in drift voltage since neither the production of electrons nor the gas amplification are directly influenced by the drift voltage.

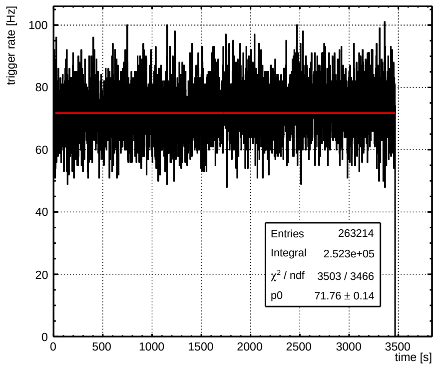

Figure 6.8: Trigger rate plotted against time. This measurement is done with 100/18 layers at $d_y = 0$ V. Additionally a fit with a 0^{th}-order polynomial (red line) was made to get the mean trigger rate.

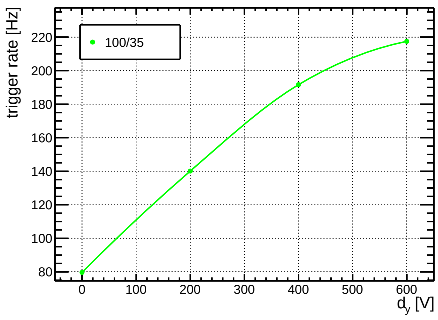

Figure 6.9: Trigger rate of the detector for different values of d_y. Data points for 100/35 converter layers are shown. The line is not a fit but is drawn for better visualisation. A linear rise with saturation for high drift voltages d_y can be observed.

6.1.3 Trigger Rate

The trigger rate is measured by the readout software mmDAQ (see section 3.4) and written in the measurement root-file. It is then plotted in a histogram against time. Such a histogram can be seen in figure 6.8. In order to retrieve the mean trigger rate a 0^{th}-order polynomial is fitted to trigger rate. All values of the trigger rate for individual measurements are obtained in this mannar and implicitly are the mean trigger rate. The error is taken from the fit error not including environmental effects since they are difficult to quantify (see chapter 8). This holds for all measurement plots, as for example in figure 6.9. Figure 6.9 shows the change in trigger rate over the change in drift voltage d_y. At first the trigger rate rises linearly with the drift voltage. For higher drift voltages saturation effects start to occur. This is due to the fact that the source is constantly emitting photons. Therefore the production rate of electrons reaching the gas is constant and at some drift voltage the rate of electron extraction and readout becomes equal to the rate of production.

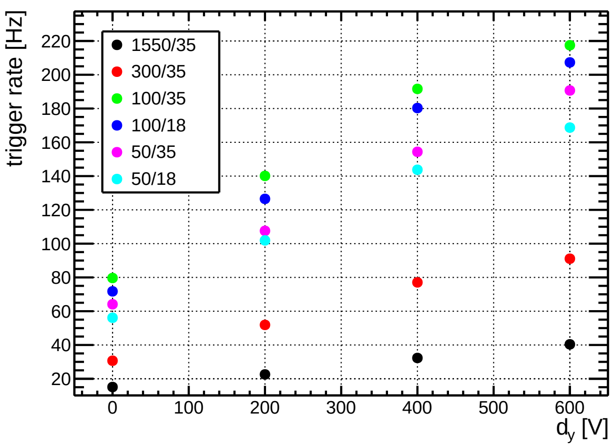

Figure 6.10: Trigger rate for different converter layer types and different drift voltages d_y. The errors are in the order of 10^{-1} Hz and therefore are overlapped by the points. All show a linear increase in the beginning with saturation effects at the end.

The performance of all layers investigated is shown in figure 6.10. There is a clear distinction between the layers made of FR4 (black and red) and the other layers made of Kapton. The worst performing layer is 1550/35 as expected since it has the most passive material of all layer types. The 300/35 layer is a factor of ≈ 2 better performing than 1550/35 since it has less FR4 absorbing radiation. The layers made of Kapton outperform 1550/35 by a factor of $\approx 4-5$ and 300/35 by a factor of $\approx 2-3$. This is due to their even thinner substrate. Within the layers with the same substrate thickness the one with 35 µm of copper outperforms the one with 18 µm copper as expected because of a little more surface area on the sides to leave the copper through. The best performing converter layer is 100/35. The reason why it is not 50/35 although having less passive material is that 50/35 and 50/18 are so thin that they are less mechanical stable. Therefore they deform more easily and their electric fields are non-optimal resulting in less efficient electron guiding.

6.2 Simulation Results

The simulations are done as described in chapter 5. In the following some additional simulation results comparing the different converter layer types are presented.

6.2.1 Electron Production Distribution

The 2D production distribution of electrons produced in the simulation can be seen in figure 5.3. In order to better compare the different layers the profile in X-direction for multiple layers is depicted in figure 6.11. The layer positions can be seen by the minima in X-direction. As expected, the minima become less and less dominant for thinner layers. For 1550/35 and 300/35 they are clearly visible with 1550/35 having wider minima as 300/35. The 100/18 layers have very weak minima only visible for the first to minima at $x \approx -45$ mm and $x \approx -34$ mm. 50/35 does not show any minima. This is due to the layers being even thinner than the binning of the histogram in figure 6.11. Additionally it can be seen that the $1/r^2$ decrease gets weaker for thinner layer types. A strong contrast is 1550/35 compared to 50/35 where 1550/35 although starting higher at $x \approx -48$ mm undercuts 50/35 in the region of $x > -25$ mm. This indicates more absorption happening as to be expected for 1550/35 layers as they are they have the most passive material.

6.2.2 Electron Guiding and Spatial Distribution

How the changes in the electric fields discussed in section 5.2.3 correspond to the electron end position after being successfully guided to the amplification region is seen in figures 6.12 and 6.13. Figure 6.12 shows the end positions of the electrons for all converter layer types. The minima between the peaks directly depend on the thickness of the layers. The widest minima can be seen for 1550/35 layers. The peaks become broader and lower in correlation to the width of the minima due to the integral (the total number of electrons) only varying weakly. This is caused by the electric field not strongly changing between the different layer types as shown with figures 5.10 and 5.12. Considering changes in the drift voltage d_y the effect of it on the guiding distribution in figure 6.13 becomes visible. The minima corresponding to the positions of the layers become broader for lower d_y values. In addition the peak heights increase with higher drift voltages d_y. Interestingly the peak structures do not change for different values of d_y. For example all peaks around $x \approx -2.7$ cm share the same double peak substructure. This leads to the conclusion that the changes in the electric field observed between figures 5.10 and 5.13 are rather insignificant to the end guiding distribution.

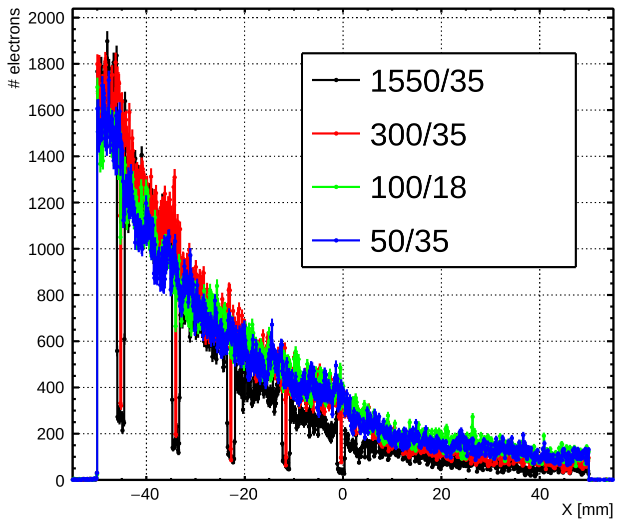

Figure 6.11: Profiles in X-direction of the production distributions for multiple converter layer types. Not all converter layer types are shown for better visibility. For all curves an $1/r^2$ decrease over X is visible.

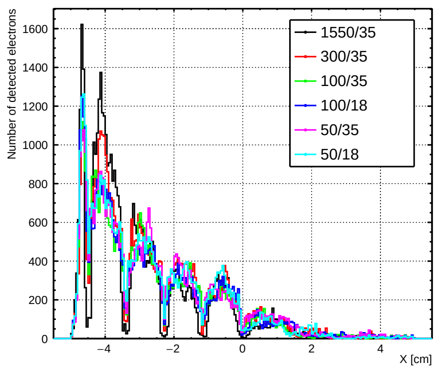

Figure 6.12: Electron end position after successful drift for all converter layers at d_y = 600 V (from [18]). All layers show a similar $1/r^2$ decrease.

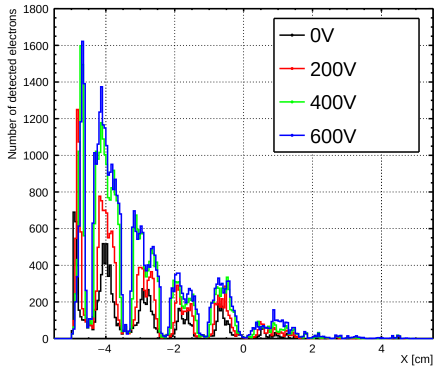

Figure 6.13: Electron end position after successful drift for 1550/35 converter layer at different drift voltages d_y (from [18]). For all d_y an $1/r^2$ decrease can be seen.

6.2.3 Trigger Rate

The simulated trigger rate is shown in figure 6.14. It is normalised to the $d_y = 0$ V value of 1550/35 layers. There are two main lines visible. The line of 1550/35 and the line comprised of all other layers. The 1550/35 layers are the least performing out of all layer types while all other layers group together and exceed 1550/35 by a factor of ≈ 1.5. 300/35 is performing the best out of all layers only being slightly above the layers made of Kapton (100/35, 100/18, 50/35, 50/18). These layers all perform the same except for statistical variations.

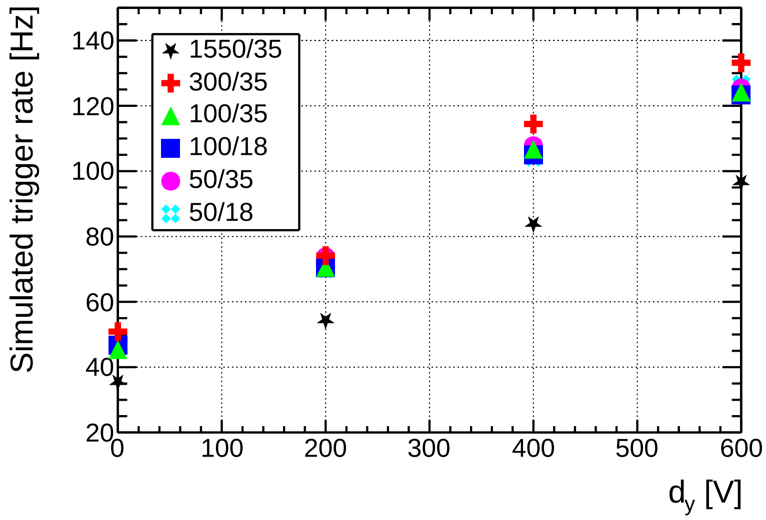

Figure 6.14: Simulated trigger rate for all converter layer types with different drift voltages d_y with a time-cut of 800 ns (from [18]). All layers start with a linear increase with saturation effects towards the end.

6.3 Comparison of Simulation and Measurement

In the following the measurement results will be compared to the simulation predictions. How the different converter layer types influence the position distributions is seen in figures 6.3 and 6.12. Comparing both, the simulation in figure 6.12 predicts a very thin and high peak at $x \approx -50$ mm while the measurements show this peak to be rather small and it is only visible in one measurement. Simulation and measurement show that the width of the minima corresponds to the thickness of the layers. But the simulation predicts the minima to become more significant for thicker converter layers which is not the case for the measurements where this effect can hardly be seen at all. The reason for the minima of 50/18 being higher than the rest is because it's measurement time is longer. Therefore more events are recorded leading to the shift of the curve. The peak structure of both are similar. The first major peaks of both are quiet sharp while the rest is relatively broad. Both show the $1/r^2$ decrease in X-direction. The last peak at $x > 0$ mm is very small in the measurements while the simulation depicts it to be significantly broader.

This and the very thin first peak in the simulation come from the fact that the electric fields in the simulation end at $x = -55$ mm as shown i.e. in figure 5.10 not considering the casing which is set to ground potential. This then leads to the electric field shown in figure 6.15.

Figure 6.15 shows the equipotential lines of the electric field in the detector considering the casing to be set to ground potential. Most importantly the equipotential lines to the left of the layers bulge out towards the casing. This would result in the electrons being guided

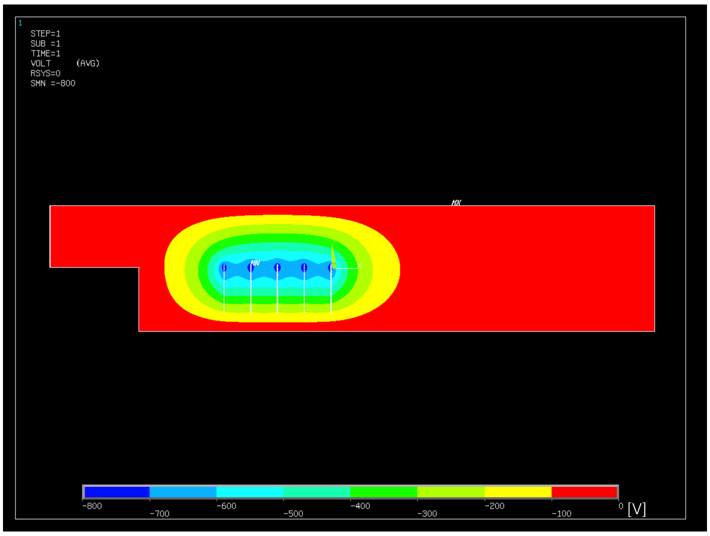

Figure 6.15: Voltage field of the electric field of 100/18 converter layers with $d_y = 600$ V considering the casing. The lines correspond to the equipotential lines of the electric field. An electron would move perpendicular to them.

stronger to the casing. Consequently the sharp first peak in figure 6.12 would turn out significantly smaller. To the right of the layers the electrons would spread out over an even larger area resulting in the last peak in the simulation being smaller. This is then more comparable to the measurement results.

Figures 6.4 and 6.13 show the resulting distributions in X-direction for measurements and simulation for different drift voltages d_y. The reason why the very first thin peak in the simulation and the last peak for $x > 0$ mm do not coincide between measurement and simulation is already discussed above. The minima in the measurements do not change their width as strong as indicated by the simulation. But the significance of the minima compared to the peaks does change as predicted by the simulation although the effect being weaker in the measurements. The peak structure is similar for both for the first peak with it's asymmetric peak structure. This holds for all d_y except of $d_y = 0$ V. In the case of all other peaks the peak structures of the measurements are broader than the ones in the simulation. The $1/r^2$ decrease of x is visible in both.

How the different converter layer types perform compared between simulation and measurement can be seen in figures 6.16 and 6.17. Both are normalised to the $d_y = 0$ V value of 1550/35 layers in order to minimise systematic errors. 1550/35 performs equally in measurement and simulation and it is the worst performing layer type in both. The next better performing layer in figure 6.16 is 300/35 while in figure 6.17 it is the best performing converter layer. All other layers in the simulation are only slightly worse than 300/35 while in the measurement they outperform 300/35 with the best performing layer being 100/35. In addition 100/35 in the measurement reaches a relative trigger rate of ≈ 14 while 300/35 only achieves ≈ 3.8. This and the huge difference in the hierarchy of the layers between simulation and measurement lead to the assumption that the simulation does not cover vital effects causing the layers made of Kapton to strongly outperform the layers made of FR4 in the measurements. This needs further investigations.

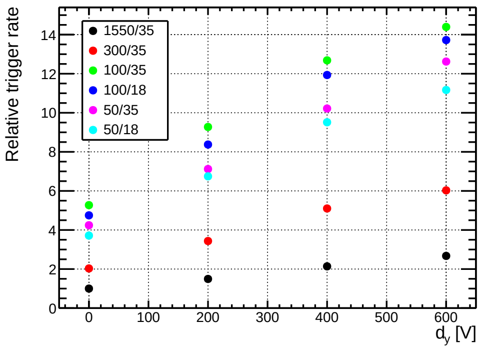

Figure 6.16: Measured relative trigger rate of all converter layer types normalised to the $d_y = 0$ V value of 1550/35. The errors are in the order of 10^{-2} and therefore are overlapped by the points. The layers perform differently but all have the same general behaviour.

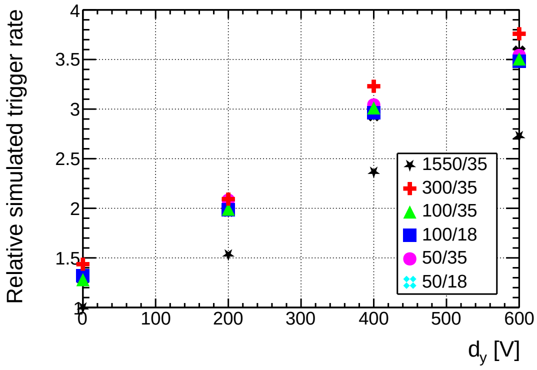

Figure 6.17: Simulated relative trigger rate for all converter layers normalised to the $d_y = 0$ V value of 1550/35 with a time-cut of 800 ns (from [18]). All layers start with a linear increase with saturation effects towards the end.

Conclusion

Simulation and measurement only agree on the behaviour of the 1550/35 converter layers. The simulation does not differ between the thinner layers. In conclusion of the measurements it is possible to improve the trigger rate of the detector up to a factor of ≈ 5 by optimising the materials of the converter layers. This leads to less passive material absorbing radiation and better guiding properties. Further possible improvements are discussed in chapter 9.

Chapter 7

Investigation of Large Layer

This chapter covers the large converter layer. Since they are about 8 cm larger than the small layers covered in chapter 6 and have wider copper strips a second, larger detector is needed. In order to make these measurements comparable to the measurements done with the other detector some small layers already discussed are remeasured with this larger detector. Additionally, an adapted support structure (see section 4.3) is designed to apply stress to the layers. Some comparisons with the results presented in chapter 6 will be made. A picture of a large layer can be seen in figure 4.7.

7.1 Measurement

7.1.1 Hit Distribution

Figure 7.1 shows the 2D hit distribution of a measurement taken with the large converter layers. It shows 5 different areas of hits corresponding to the areas between the converter layers. The first area from the right has the most hits and is not homogeneous. Subsequent areas only have very few hits but they show some variation in hit density. The line at $y = 0$ mm originates from APV (see section 3.3) effects due to one APV ending and the next one beginning. The Y-like structure with very few hits in the lower right side of figure 7.1 is caused by defect readout strips on the anode (see section 3.3). The amount by which the areas between the layers differ can be better seen in figure 7.1. Here the profile of figure 7.1 in X-direction is shown. Comparing these boxes to the minima positions they match quite well for all but for the first minima, which it is shifted to lower x-values. This probably is a result of the first layer being bend although put under stress. Due to the high amount of copper on these large layers (see section 4.2.2) the stress achievable with the support structure (see section 4.3) is not sufficient to pull them totally straight. Some amount of curvature still remains causing the minima to move since the electric field is no longer homogeneous. The large amount of copper causes strong absorption of radiation leading to the very strong $1/r^2$ decrease seen in figure 7.2. The first two peaks from the right between the converter layers show some substructure. This substructure is potentially caused by the upper readout strips (see section 3.3) which run in X-direction. But the periodicity of the readout strips is higher than the effect visible in the peak substructure. The fact that this substructure does not appear for the lowest three peaks may hint towards this effect originating in the radiation since the latter layers are strongly shielded by the previous layers. This is not seen for the smaller converter layers since they have an relative area coverage between Kapton and copper strips of 50%/50% while the large layers have coverage of 10%/90%. The two one bin wide peaks around $x \approx 0$ mm probably are APV or readout strip defects.

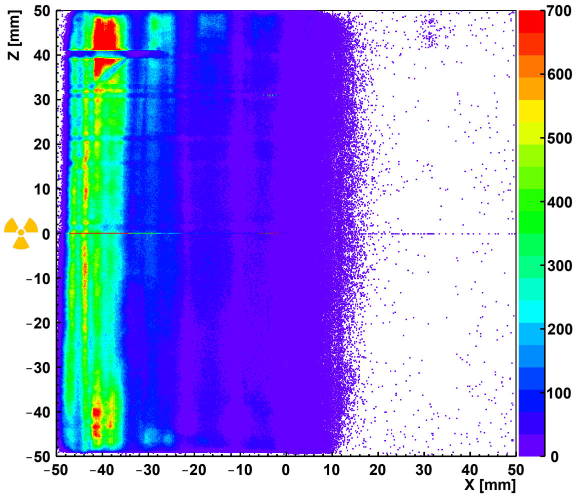

Figure 7.1: Measured 2D hit distribution of the large converter layer with d_y = 1150 V. The source is positioned at $(X, Z) = (-78.25, 0)$ [mm] indicated by the radioactive symbol. The areas between the layers can be distinguished.

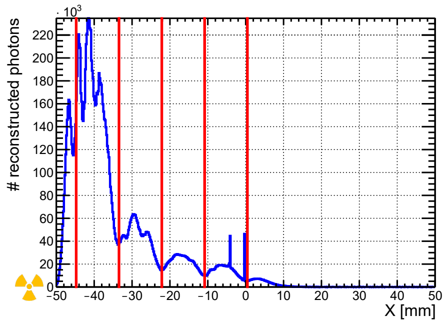

Figure 7.2: Profile in X-direction from figure 7.1 with $d_y = 1150$ V. The red boxes indicate the layer positions and thickness. The source is at $X = -78.25$ mm indicated by the radioactive symbol. A strong $1/r^2$ decrease is visible.

7.1.2 Cluster Charge

The cluster charge distributions introduced in section 6.1.2 depend on the readout electronics including the used APV chips (see section 3.3). In order to compare the measurements with the large converter layers to the results of the other layers some of the small layers have be remeasured with the large detector and it's APV chips to obtain comparable results.
The cluster charge for the large layers with different drift voltages d_y is seen in figure 7.3. For all voltages the charge shows a broad peak at $\approx$ 3500 adc channels with a long tail towards higher charges. For $d_y \leq 1000$ V the peaks move to lower charges of $\approx$ 3000 adc channels In figure 7.4 the cluster charge distribution for the large layers compared with other layers is depicted for $d_y = 200$ V. This value is chosen because a $d_y = 1000$ V for the large layer equates to $d_y = 200$ V for the normal layers due to the large layers being a factor of 5 times larger while having the same amount of strips therefore the electric field gets spread over 5 times the distance. This then leads to all layers having the same absolute electron guiding field strength. The 100/35 layers have the same peak structure and position as the large layers. 100/35, 50/35 and 100/18 seem to have two peaks where the first dominant peak nearly totally overlaps the second smaller peak. This second peak is best visible for 100/35. 50/35 is shifted towards higher charges with the main peak sitting at $\approx$ 3500 adc channels.
Compared to figure 6.6 the peak positions have not changed but the peak structure differs. This is further illustrated by figure 7.5 showing 100/18 layers measured with the small and the large detector. The small detector measurement shows the double peak structure while the large detector only resolves one broad peek. This might be caused by a lower energy resolution of the large detector resulting in the peaks getting blurred and thereby seem to be one peak. This needs further investigations.

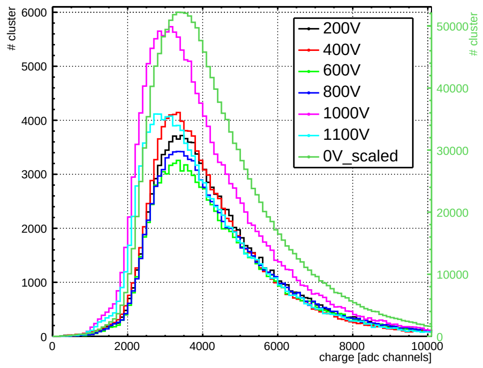

Figure 7.3: Cluster charge for large converter layers with different drift voltages d_y. The measurement with $d_y = 0$ V is scaled to be comparable since it has significantly more recorded events. For all values of d_y a broad peak with a long tail can be seen.

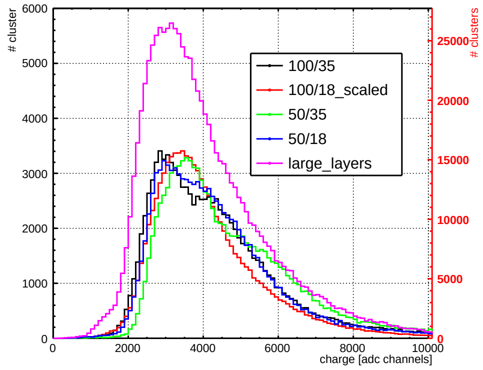

Figure 7.4: Cluster charge for all layers measured with the big detector for a drift voltage of $d_y = 600$ V. The measurement with 100/18 layers is scaled to be comparable since it has significantly more recorded events. All layers have a broad peak with a long tail.

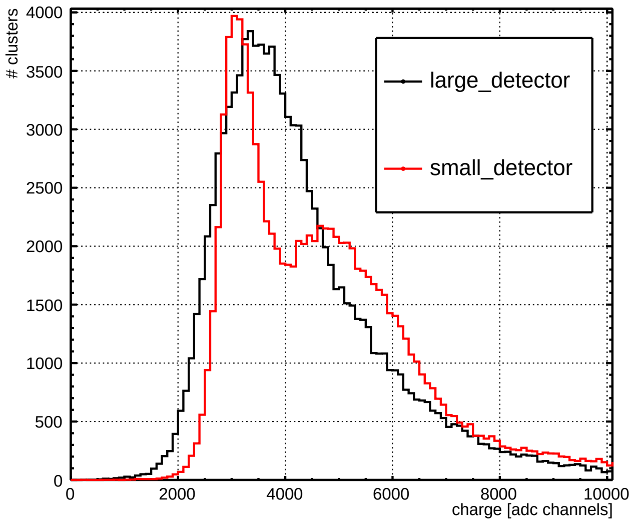

Figure 7.5: Cluster charge of 100/18 converter layers in both detectors. Both measurements are done with $d_y = 600$ V. For the large detector one broad peek is visible while for the small detector there is a double peak structure.

7.1.3 Trigger Rate

Figure 7.6 shows the measured trigger rate while using the large layers with different drift voltages d_y. All points correspond to the mean trigger rate obtained by the same procedure as described in section 6.1.3. Higher voltages are not investigated because the top of the layers have a distance to the casing of only $\approx$ 1.2 cm. Since the casing is put to ground potential and the top of the layers has $\approx$ 3 kV at $d_y = 1100$ discharges do not allow higher values of d_y. The trigger rate rises for higher d_y with a dip at $d_y = 400$ V. This rise is not very smooth because strong weather and therefore atmospheric pressure changes influenced the trigger rate even within the measurements resulting in the fits to be non-optimal. For further details on the influence of atmospheric pressure on the measurements see chapter 8. This leads to the individual points varying but it does not disturb the general trend or order of magnitude of the trigger rate. They have a poor performance considering they have a large amount of copper and should produce a large quantity of electrons. A possible explanation is that the guiding is very inefficient. This is discussed in section 7.2.2.

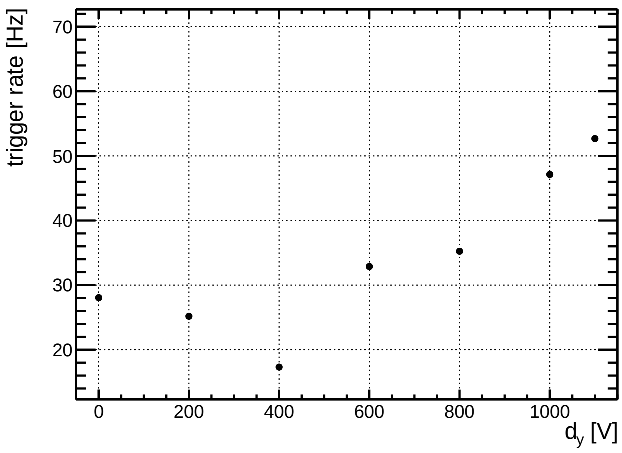

Figure 7.6: Trigger rate of the large layers for different drift voltages d_y. All points are mean values got by the same method as described in section 6.1.3. The errors are in the order of 10^{-1} and therefore are overlapped by the points. The data points are scattered but in general increase for higher values of d_y.

7.2 Simulation Results

The simulations are done as described in chapter 5. In the following some additional simulation results comparing the different converter layer types are presented.

7.2.1 Electron Production Distribution

The production distribution of electrons when simulating large converter layers is shown in figure 7.7. A radial distribution is visible caused by the radially emitting source. The positions of the layers can not be seen since they are very thin (they have the same dimensions as the 50/18 layer type) such that they do not produce minima by absorbing radiation and electrons. But the large area covered by copper makes the layers visible in figure 7.8. Here the layer positions can be identified by the small peaks in the constantly decreasing distribution towards high values of x. It does not really show an $1/r^2$ decrease because the electrons produced in the copper strips dominate the area between the the layers leading to a step-like structure.

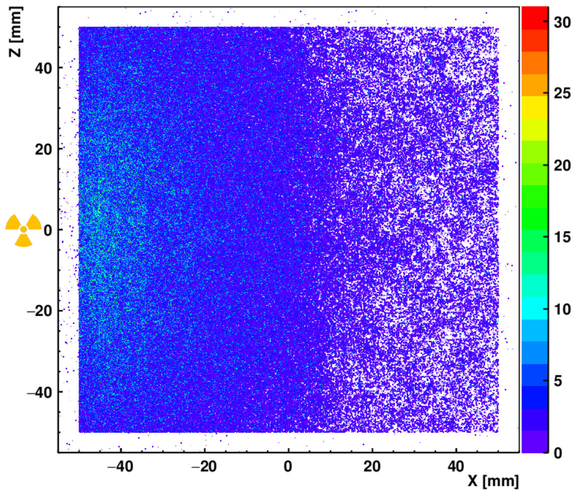

Figure 7.7: Production XZ-position of all electrons reaching the active gas volume simulated for large converter layers. The source is positioned at (X,Z)=(-78.25,0) [mm] indicated by the radioactive symbol. A radial distribution can be seen.

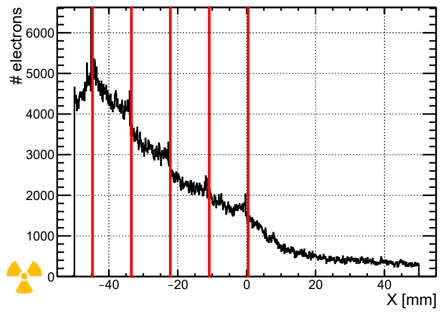

Figure 7.8: Profile in X-direction of the production distribution in figure 7.7. The source is positioned at $X = -78.25$ mm indicated by the radioactive symbol. An somewhat linear decrease with an exponential ending is visible.

7.2.2 Electron Guiding and Spatial Distribution

The electric field between the large layer is depicted in figure 7.9. It shows the voltage field with the equipotential lines for $d_y = 600$ V. An electron moves perpendicular to these lines. The field is very homogeneous in between the layer with slight deformations at the lower end of the layers due to the drift field below the layers pushing into the layer area.
The resulting distributions of the electrons after a successful drift with different drift voltages d_y is shown in figure 7.10. An electron counts as detected if it reaches $y = -5.1$ cm within the time-cut of 800 ns. This time-cut is chosen to be the same as for the small layers in section 6.2.2 since the readout electronics are also the same. In figure 7.10 all d_y behave the same way with 6 peaks. These peaks are in the middle of two converter layers or at the boundary of the simulated electric field. The difference between the drift voltages is only statistical. The second peak from the right is the highest for all of them. The subsequent peaks get broader and smaller. The reason for the decrease for lower values of x is the radial dependence of the initially produced electrons as seen in figure 7.7 and figure 7.8. Figure 7.11 shows the starting positions in the XY-plane of the electrons that reach the detection limit. Interestingly only electrons with $y \lesssim -3.8$ cm get detected. This mainly is influenced by the time-cut. It also suggests that the guiding is very inefficient.
Due to the already poor guiding it would not result in a noticeable change if the casing is considered in the electric field simulation depicted in figure 5.2.
The electric field produced by the large layers with $d_y = 1000$ V has a field strength of only 100 V/cm. This is due to the height of $h_L = 10$ cm of the large layers. The small layers have the same electric field strength for $d_y = 200$ V since they are only 2 cm in height. The

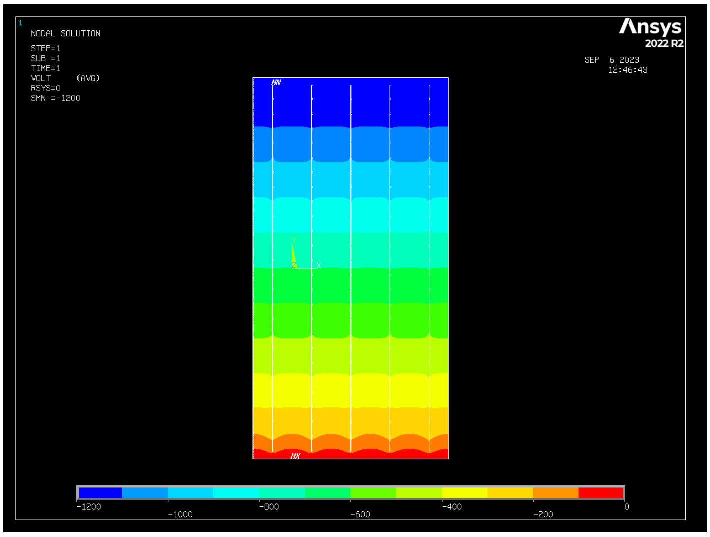

Figure 7.9: Voltage field for the large layers for d_y = 600 V. The lines correspond to the equipotential lines. An electron would move perpendicular to these lines. The field is quite homogeneous.

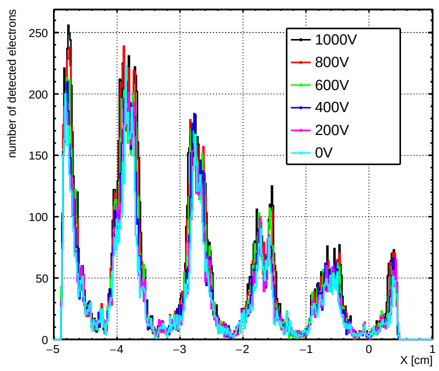

Figure 7.10: End positions of electrons in X-direction for different drift voltages d_y for large converter layers with a time-cut of 800 ns. A weak $1/r^2$ decrease can be seen for all d_y.

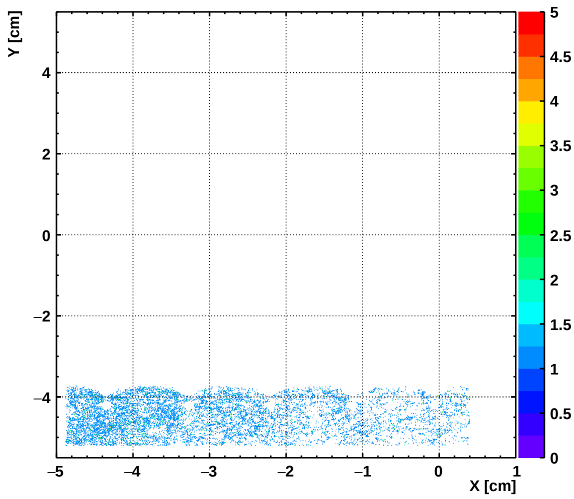

Figure 7.11: Starting positions of electrons that successfully reach the extraction limit with d_y = 1000 V within the time-cut of 800 ns. Only electrons at the bottom are extracted.

maximum field strength for the small layers is 300 V/cm for $d_y = 600$ V. Scaled to the large layers this would correspond to $d_y = 3000$ V. This is not simulated because it could not be measured without constantly discharging.

7.2.3 Trigger Rate

The simulated trigger rate is obtained by calculating the production efficiency and the guiding efficiencies which are then multiplied with the activity of the source used in the measurement. The result is shown in figure 7.12. The trigger rate increases linearly with rising drift voltage d_y. There is no saturation visible although the trigger rate shows weak saturation for the small layers in section 6.2.3. The reason for this is the larger height of the large layers resulting in weaker electric field strength at the same drift voltage d_y. Therefore, $d_y = 1000$ V for the large is equal to $d_y = 200$ V for the small layers. In this context it is not surprising to not see saturation effects.

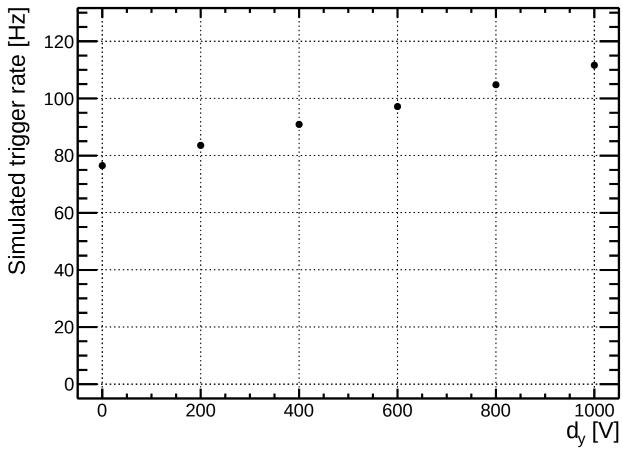

Figure 7.12: Simulated trigger rate for large converter layer with different drift voltages d_y and a time-cut of 800 ns. The rate rises linearly with increasing d_y.

7.3 Comparison between Simulation and Measurement

Comparing the measured hit distribution in X-direction for the large converter layers with $d_y = 1000$ V in figure 7.13 with the corresponding simulation in figure 7.14, the peaks in the measurement are broader than in the simulation and the $1/r^2$ decrease is significantly stronger in the measurement. Additionally, the first peak in the measurement is more dominant than in the simulation. It seems like the first two peaks in the simulation are combined to one big peak in the measurement. Without the layer indicators the very first peak could be mistaken to be a part of the peak at $x \approx -40$ mm. The first two peaks in figure 7.13 have three sub-peaks while the rest has only one broad peak. The minima between the peaks are more dominant in the simulation (figure 7.14) than in the measurement (figure 7.13) where the minima between the smaller peaks are less pronounced. The one bin wide peaks in the measurement at $x < 0$ mm are probably readout defects. The $1/r^2$ decrease of peak heights is significantly stronger in the measurement than in the simulation. This might indicate that the simulation is not accounting for the right amount of absorption in either the copper or the Kapton.

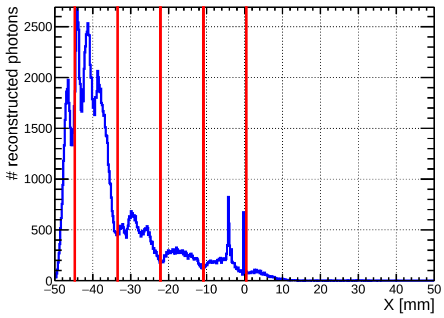

Figure 7.13: Measured profile in X-direction of a measured hit distribution with large converter layers and a drift voltage of $d_y = 1000$ V. A strong $1/r^2$ decrease can be seen.

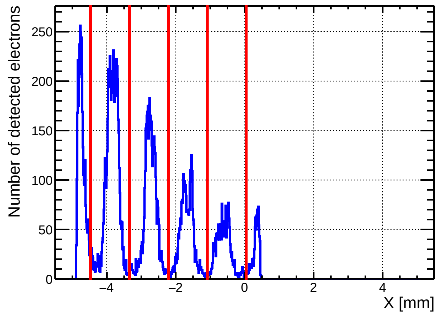

Figure 7.14: Simulated end positions of electrons in X-direction for a drift voltage of $d_y = 1000$ V for large converter layers with a time-cut of 800 ns. The $1/r^2$ decrease visible is rather weak.

The measured relative trigger rate is compared with the simulated relative trigger rate in figure 7.15. The measured values are increasing for larger values of d_y but single points deviate from this behaviour for reasons discussed in section 7.1.3. The simulation depicts the ideal behaviour of linear increase for higher drift voltages. The largest difference except for the point at $d_y = 400$ V is $\approx 25\%$ at $d_y = 1000$ V. This is acceptable considering the error does not cover environmental effects since they are difficult to quantify. Although the simulation is monotonically rising and is ending at a relative trigger rate of ≈ 1.46 the measurement surpasses it with ≈ 1.7 at $d_y = 1000$ V.

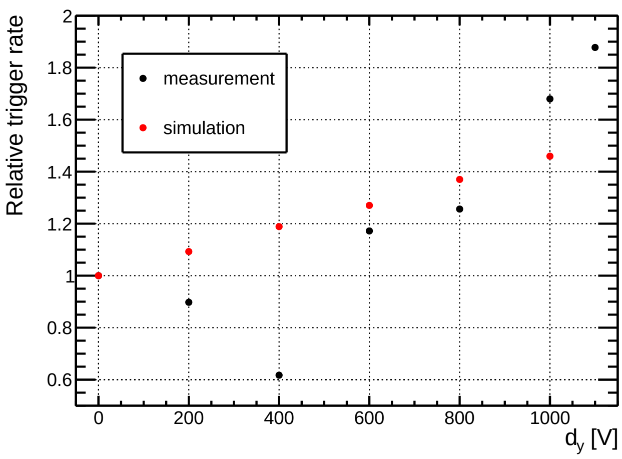

Figure 7.15: Measured and simulated relative trigger rate for large converter layer with different drift voltages d_y. The measurement errors are in the order of 10^{-2} and therefore are overlapped by the points. The simulation time-cut is 800 ns. The points are normalised to the trigger rate at $d_y = 0$ V. Both show the same general trend of increasing for higher d_y.

7.3.1 Conclusion

The large layers perform moderately mainly due to their sub-optimal electron guiding. This could be improved by reducing the height to be similar with the small layers. Because of the larger amount of copper it converters already a large amount after the first layer (see figure 7.13) with which a "one converter layer" setup may be possible in future.

7.4 Comparison between Small and Large Layers

An important point in the comparison of the small and the large layers is to account for the larger angular coverage the large layers have. See figure 7.16 for a sketch of the parameters used to calculate the correction factor.

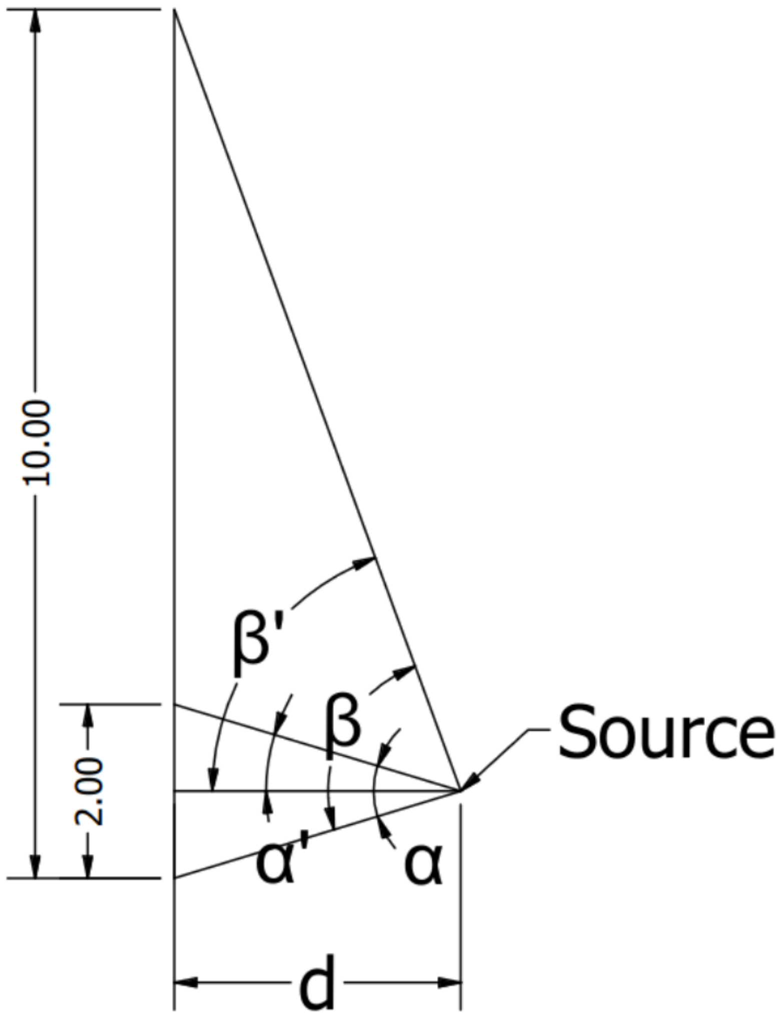

Figure 7.16: Sketch of the angular coverage of the small layers (2 cm) and the large layers (10 cm). It is to scale for the first layer with $d = 3.3$ cm. The source is positioned to the right.

The parameters used are defined as

$$\alpha' = \arctan(\frac{1\text{cm}}{d}) \tag{7.1}$$

$$\alpha = 2 \cdot \alpha' \tag{7.2}$$

$$\beta' = \arctan(\frac{9\text{cm}}{d}) \tag{7.3}$$

$$\beta = \alpha' + \beta' \tag{7.4}$$

The factor δ of additional radiation absorbed is then the ratio between the angles covered by the large and small layer

$$\delta = \frac{\beta}{\alpha} = \frac{\alpha' + \beta'}{2\alpha'} = \frac{\alpha'}{2\alpha'} + \frac{\beta'}{2\alpha'} = \frac{1}{2} + \frac{\beta'}{2\alpha'} \tag{7.5}$$

With the definitions in equations 7.1 and 7.3 as a factor of the distance d to the source δ is described by

$$\delta = \frac{1}{2} + \frac{\arctan(\frac{9\text{cm}}{d})}{2\arctan(\frac{1\text{cm}}{d})} \tag{7.6}$$

The performance P' of the large layers projected on the height of the smaller layers is then

$$P' = \frac{P}{\delta} \tag{7.7}$$

with P being the measured performance. With the distance of the converter layers to the source the resulting values are:

# layer	d [cm]	δ	$1/\delta$
1$^{\text{st}}$ layer	3.3	2.57	0.389
2$^{\text{nd}}$ layer	4.5	3.03	0.330
3$^{\text{rd}}$ layer	5.7	3.40	0.294
4$^{\text{th}}$ layer	6.9	3.68	0.271
5$^{\text{th}}$ layer	8.1	3.91	0.256

Table 7.1: Correction factor δ for large converter layers for each individual layer position in the setup

In order to compare the measurements done with the big detector to those done in the small detector (see chapter 6) a normalisation has to be done. This is the reason for remeasuring a couple of the small layers. The trigger rates are draw in figure 7.17. The drift voltages for the large layers are adapted to larger height of the layers in order that same values of d_y represent same electric field strengths. The large layers perform the worst out of all layers. The best performing layer is 50/35. Compared to the measurements in the small detector seen in figure 6.10 the hierarchy of the layers with 100 µm of Kapton and the layers with 50 µm of Kapton is flipped and 100/35 and 50/18 now perform the same towards the higher d_y. Therefore a normalisation of the two detectors is not possible.
If one could normalise the large detector and even if one underestimates the correction factor δ for all layers to be 2.57 the large layer will probably even underperform the 1550/35 layers when divided by δ. Maybe a layer of it's design could perform better if it is only 2 cm high like the other converter layers. Another option would be an insulation towards the casing in order to operate the large layers at higher drift voltages d_y. This could lead to drift field strengths comparable to $d_y = 600$ V for the small layers.

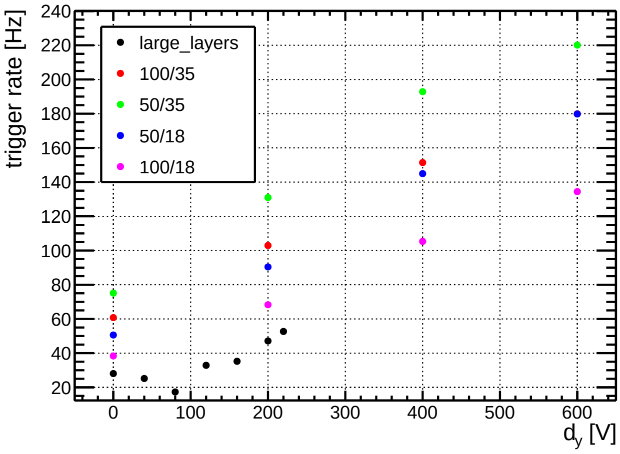

Figure 7.17: Trigger rate of converter layers measured with the large detector with different drift voltages d_y. The values of d_y for the large layers are adapted to represent the same electric field strength accounting for the larger height of the layers. The errors are in the order of 10^{-1} and therefore are overlapped by the points. All layers perform differently but show a increase towards higher values of d_y.

Chapter 8

Environmental Effects

In this chapter the influence of temperature, pressure and gas humidity on the measurements is further investigated with Garfield++ simulations and a long time measurement. The reason for this investigation can be seen in figure 8.1. There the same converter layers (see chapter 4) in the same detector perform differently on two separate dates.

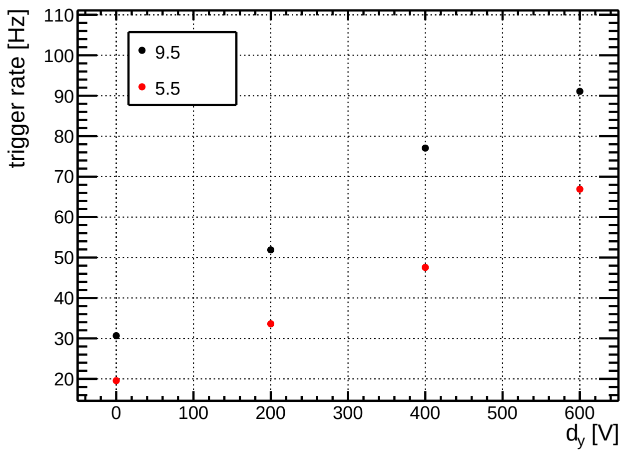

Figure 8.1: Measurements of 300/35 converter layers for different drift voltages d_y a two different dates. The errors are in the order of 10^{-1} and therefore are overlapped by the points. The measurement done on the 5.5 is significantly lower than the one taken on 9.9 .

8.1 Simulation

Since pressure and temperature influence the kinematics of the electron guiding a simulation is done varying both. The results can be seen in figure 8.2. It shows that guiding becomes more efficient for high pressure and low temperature as expected because both lead to less collisions of the electrons. At low temperatures T the mean thermal velocity of the electrons $v \propto \sqrt{T}$ is low. In addition the mean free path $\lambda \propto T/p$ decreases for high pressure p and low temperature T. These are dependencies of the diffusion coefficient $D \propto \sqrt{T^3}/p$ resulting in less diffusion of the electrons [7]. Thereby there is less chance of them hitting the converter layers. But the change in guiding efficiency only spans $\approx 0.7\%$. In conclusion the simulation expects the effect of pressure and temperature on the guiding to be negligible.

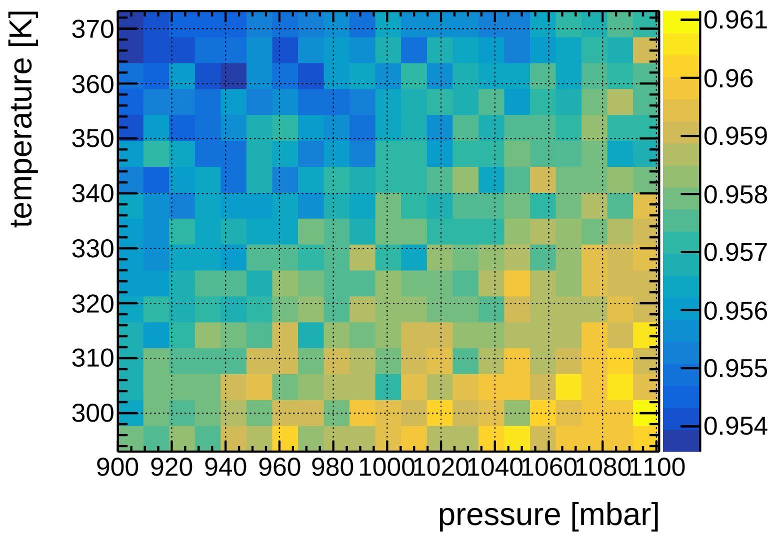

Figure 8.2: Guiding efficiency for different combinations of temperature and pressure. The efficiency has it's maximum at high pressures and low temperatures.

8.2 Measurement

In order to check the simulation predictions a long time measurement with the large converter layers (see section 4.2) at a drift voltage of $d_y = 1150$ V is done. This drift voltage is the highest achievable d_y without discharges occurring. The result is shown in figure 8.3.

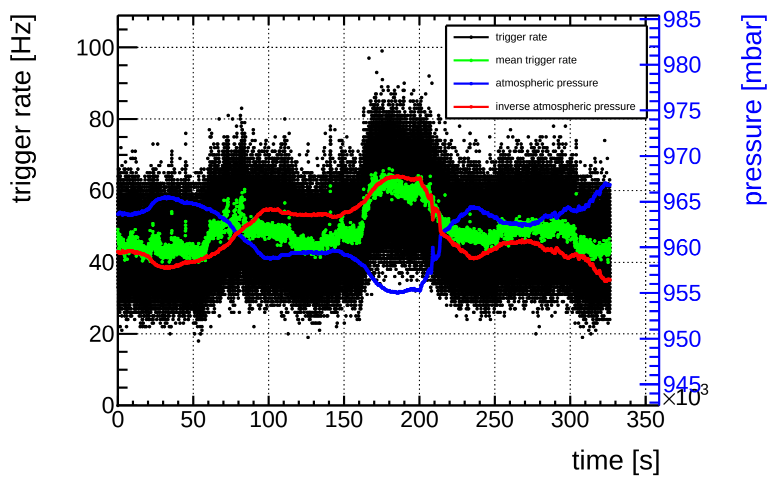

Figure 8.3: Long time measurement with large converter layers and $d_y = 1150$ V. Pressure data from [26]. The green points are the mean over 60 seconds of the trigger rate. Note that the pressure scale only holds for the non-inverted curve. The inverted pressure and the trigger rate show a very similar behaviour.

In figure 8.3 the trigger rate development over time is depicted. In addition the atmospheric pressure during the measurement is plotted. To narrow down the trigger rate a mean over 60 seconds is taken resulting in the green points. Interestingly the trigger rate shows an anti-correlation with the pressure. To further illustrate that the blue pressure curve is inverted resulting in the red curve. Comparing the green points with the red curve one sees that they match. They match especially well at the peak for $170 < t < 210$ [10^3·s]. While the pressure varies in a range of ≈ 12 mbar the trigger rate changes by $\approx 50\%$. This effect is higher than the effect expected by the simulation. A possible reason for this could be that the mean cluster charge changes with the pressure indicated by figure 8.4 [27].

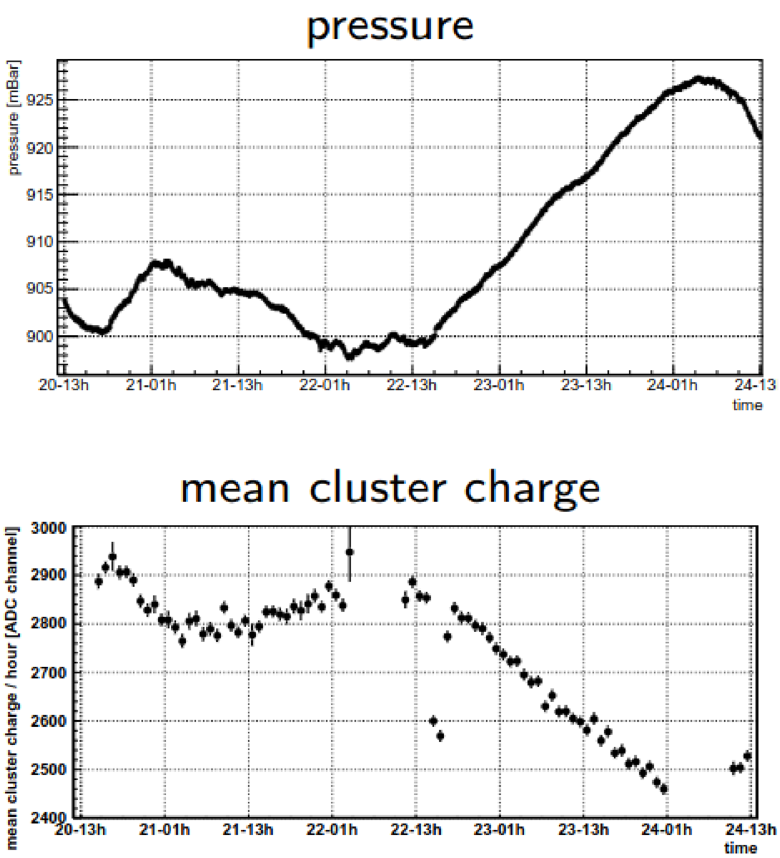

Figure 8.4: Pressure and mean cluster charge correlation plotted against time (from [27]). An anti-correlation can be observed.

Considering the constant discriminator in the trigger signal electronics (see section 3.3) a change in the mean cluster charge would lead to more or less events surpassing the discriminators threshold and thereby influence the rate of trigger signals. The mean of the cluster charge distribution (see section 7.1.2) for different times during the measurement shown in figure 8.3 is depicted in figure 8.5. It does not seem to be anti-correlated to the pressure. Additionally the variation in the mean charge is weaker as expected from figure 8.4. The reason could be that figure 8.4 is made with landau distribution in cluster charge produced by muon irradiation. Either way this pressure dependency needs further investigation. In the meantime this dependency should be eliminated since the trigger rate is a crucial value for the measurements and should not be influenced by environmental conditions. A possibility would be to implement a pressure stabilisation mechanism at the end of the gas line. This would then hold the pressure on some constant value which is higher than maximum expected atmospheric pressure.

8.2.1 Gas Humidity

The following section will discuss the effect of water contamination of the detector gas on the measurements. Figure 8.6 shows the typical gas humidity development of time. The gas humidity for all measurements starts at $\approx 500 \pm 100$ ppm. The starting point mainly depends on the time the detector spend flushing with gas after reassembly between measurements with

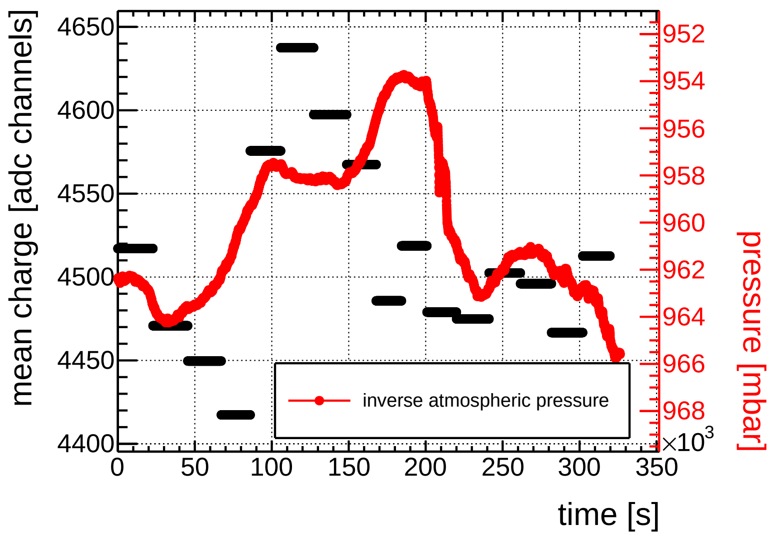

Figure 8.5: Mean value of the cluster charge distribution of the measurement shown in figure 8.3. The absolute value of the mean is not relevant. The mean is taken over 1 million events each. This results in the different time lengths of the means when combined with the trigger rate. No real correlation can be seen.

different converter layer types. This also explains the slow decrease over time since more water contaminants get flushed out of the detector. The end point then depends on the gas tightness of the detector, of the gas line and of other detectors in the gas line. Figure 8.7 shows the trigger rate development over time for the same measurement as in figure 8.6. At this low contamination level the trigger rate does not show any dependence on the gas humidity.

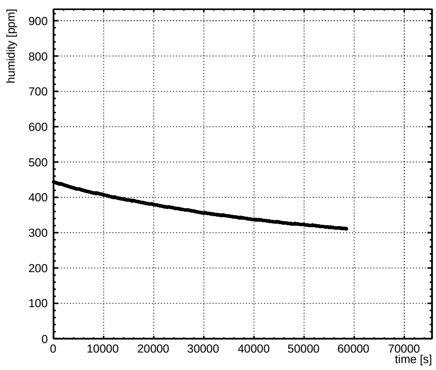

Figure 8.6: Exemplary plot of gas humidity over measurement time. It begin at a relatively low value and further decrease gradually over time. Shows the same measurement as figure 8.7.

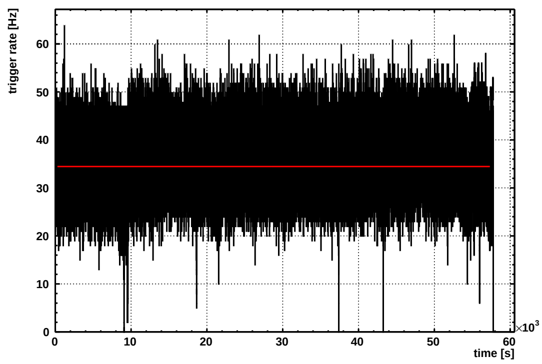

Figure 8.7: Exemplary of the trigger rate plotted against time. Additionally a fit with a 0^{th}-order polynomial (red line) was made to get the mean trigger rate. The trigger rate stays constant. Shows the same measurement as figure 8.6.

Chapter 9

Optimisation of Converter Layer Material

In this chapter simulations are presented which vary some parameters of the converter layers (see chapter 4). This is done to investigate further improvement possibilities in the layer geometry and material composition. The simulations are done with Geant4 with 10 million photons in the manner described in chapter 5. The total efficiency is calculated by dividing the number of events with a least one electron reaching the active gas volume by the number of events in which the photon enters the active gas volume (≈ 1.6 million).

9.1 Material Thickness

In figure 9.1 the thickness of the strips and the thickness of the Kapton are altered. Additionally gold is compared to copper as a converter strip material. The triangles indicate a change in Kapton thickness for copper and gold as the strip material. Both show that the thickness of Kapton does not influence the efficiency. The points with gold naturally have a higher efficiency because gold has a higher atomic number Z than copper and therefore converts more photons into electrons by the photoelectric effect (see equation 2.4).
For the thickness variation of copper strips the efficiency rises fast until a thickness of ≈ 10 µm. Then it reaches a plateau for a thickness off $\approx 20 - 30$ µm while slowly decreasing afterwards. The steep rise at the beginning is caused by the limited range of electrons in copper already discussed in section 5.2.2. Towards larger thicknesses the absorption of photons without electrons reaching the gas becomes more and more dominant. These effects are even stronger for gold. The rise at the beginning already stops after 2 µm and the exponential absorption decrease is clearly visible due to much higher atomic number of gold. After a thickness of ≈ 30 µm gold performs worse than copper because of the absorption strongly dominating. The plateau of the black points reaches the efficiency of the standard 300/35 converter layers. This is not reflected in the measurements where 50/18 layers outperform 300/35 layer by far (see section 6.3). The standard 1550/35 layers are as expected only outperforming strongly non-optimal variations. In any case all converter layer types are better than not having any converter layers. The copper strips find their maximum at ≈ 1.9 times better than no layers and the gold strips outperform no layers by a factor of ≈ 2.7. The investigated converter layers (see chapter 4) with 18 µm or 35 µm of copper already lie in the maximum for copper. Layers with gold converter strips would have to be very thin in order to outperform the copper converter strips.

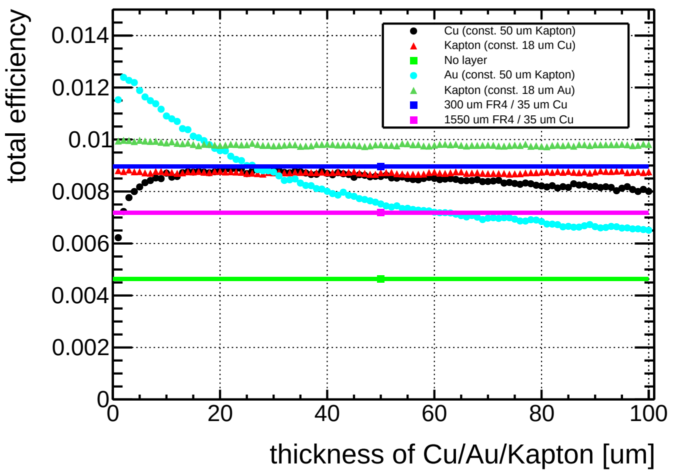

Figure 9.1: Simulated total efficiency for converter layers with varied parameters: the strip thickness for copper and gold (dots), the substrate thickness made of Kapton for strips of copper and gold (triangles) and reference efficiencies (squares). The comments in the brackets indicate unchanged variables.

9.2 Strip Width

Figure 9.2 shows the change in total efficiency for variations of the converter strip width and material. For both copper and gold the efficiency rises with increasing width. This is because of more area to convert photons into electrons without decreasing the probability of the electrons not reaching the gas. The little dip at the end for widths of ≈ 800 µm is due to the individual strips joining together and thereby becoming one solid plate. This leads to the surface area between the strips getting lost and therefore the electrons are slightly less likely to extract from the copper. A solid plane is not useful since no drift voltage is applicable due missing resistors. At their peak copper outperforms no layers by a factor of ≈ 2.5 and gold with a factor of ≈ 2.7. Compared to the currently used value of 400 µm the copper strips could be improved by ≈ 36% for a width of < 800 µm.

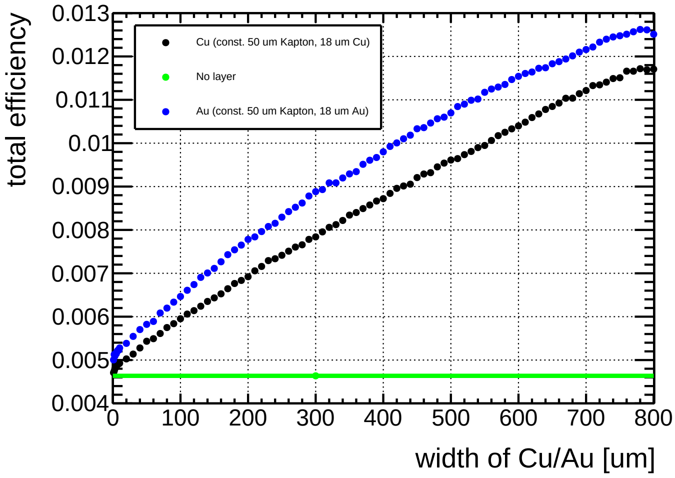

Figure 9.2: Simulated total efficiency for converter layers with varied width of the strips for copper and gold. The green line is for reference with no layer simulated. The comments in the brackets tells what is left unchanged. The lines for copper and gold rise for increasing width.

9.3 Conclusion

The current converter layer designs (see section 4.2) could be improved by using thin gold strips instead of copper strips and by making the strips wider. The combination of both could yield an relative improvement of $\approx 80\%$.

Chapter 10

Summary

In this thesis the aim is to improve the detection efficiency of photons with an energy of ≈ 60 keV for Micro-Pattern Gaseous Detectors (MPGDs). MPGDs consist of an anode and a cathode separated by a gas volume. This gas volume is divided into a drift region and an amplification region. In this thesis GEM foils are used for amplification. These foils consist of thin copper plates on a Kapton foil with small holes in periodic pattern. Voltage differences between both sides result in high electric fields in the holes resulting in electron multiplication (see chapter 3). The photon conversion improvement is achieved by inserting and optimising solid converter layers in the gas volume. These are made of high-Z material i.e. copper to enhance the interaction probability with photons. The layers consist of a substrate with metal strips on either side with resistors in between them producing a voltage gradient. Different converter layers geometries are investigated subdivided in small (2 cm) and large (10 cm) layers (see chapter 9) with the large layers having wider strips and a larger total height. Measurements are compared with simulations to understand the underlying physics. The simulation software used is Geant4, ANSYS and Garfield++ (see chapter 5). The measurements are done with a ^{241}Am source inside the detector while the detector is placed in a climatised cabinet, reducing environmental effects. Two detectors are used accommodating for the size of the small and large converter layers. The performance of a converter layer type is measured by the achieved trigger rate.
Considering the different small converter layer types the layers made of 100 µm Kapton with 35 µm thick copper strips perform the best. This layer type reaches an increase of a factor of ≈ 5 (see section 6.1.3). The simulation does not agree on this performance increase predicting all layers other than the thickest to perform basically the same at a factor of ≈ 1.4 (see section 6.3). The reason for this discrepancy needs further investigations.
The large layers covered in chapter 7 are not showing the performance expected by their large amount of copper. This is due to their poor electron guiding efficiency in combination with only low drift voltages achievable (see section 7.2.2) because of discharges above a certain drift voltage.
Environmental effects influence the measured trigger rate and thereby the performance of the converter layers as shown in chapter 8. While the simulation predicts only a weak dependence on pressure and temperature the measurements show a strong correlation with the atmospheric pressure. This is possibly caused by a change in the amount of produced charge but still needs further investigations for more insight. Humidity in the gas at values around ≈ 400 ppm shows no visible effect on the performance (see section 8.2.1).
The energy reconstruction is done by comparing the collected charge of an event. This is possible because the detector is a proportional counter. The charge is counted per electron cloud, called cluster, reaching the readout. Due to having multiple converter layers in a distance of ≈ 1 cm finite range effects become relevant. The detected cluster charge no longer

represents the total energy of an incident electron but the energy loss over 1 cm (see section 6.1.2). This inverts the expected energy distribution from simulation.
One of the most important points the simulations showed is that only a very small amount of electrons produced in the converter layers actually reach the gas and get detected. The effective range of electrons in the copper strips is ≈ 5 µm (see section 5.2.2). All additional copper only contributes weakly according to simulations.
Due to production limitations only specific material thicknesses for converter layers are investigated. Simulations altering the material, thickness and width of the converter strips show that the performance of the investigated converter layers could be additionally improved by $\approx 80\%$ if using very thin, very wide strips made of gold (see chapter 9). This could be investigated in the future.

Bibliography

[1] Konrad Kleinknecht. *Detektoren für Teilchenstrahlung.* 5th ed. Teuchner Studienbücher Physik, 2005.

[2] M.J. Berger et al. *XCOM: Photon Cross Sections Database.* URL: https://www.nist.gov/pml/xcom-photon-cross-sections-database (visited on 01/09/2023).

[3] Kazushi Terada et al. 'Measurements of gamma-ray emission probabilities of 241, 243Am and 239Np'. In: *Journal of Nuclear Science and Technology* 53.11 (2016), pp. 1881–1888. DOI: 10.1080/00223131.2016.1174167. eprint: https://doi.org/10.1080/00223131.2016.1174167. URL: https://doi.org/10.1080/00223131.2016.1174167.

[4] Emilio Segrè et al. *Experimental nuclear physics. volume I.* New York:John Wiley & sons; London:Chapman & Hall, 1953.

[5] Enrico Fermi. 'The Ionization Loss of Energy in Gases and in Condensed Materials'. In: *Phys. Rev.* 57 (6 Mar. 1940), pp. 485–493. DOI: 10.1103/PhysRev.57.485. URL: https://link.aps.org/doi/10.1103/PhysRev.57.485.

[6] W.H. Barkes and M.J. Berger. In: *Nuclear Science Series Report 39* (1964).

[7] William R. Leo. *Techniques for Nuclear and Particle Physics Experiments. A How-to Approach.* 2nd ed. Springer-Verlag Berlin Heidelberg, 1994. DOI: 10.1007/978-3-642-57920-2.

[8] A.C. Melissinos. *Experiments in Modern Physics.* Academic Press, 1966.

[9] Sir John Townsend. *The theory of ionization of gases by collision.* London: Constable & Company Ltd, 1910. URL: https://www.biodiversitylibrary.org/item/63554.

[10] H. Raether. *Electron Avalanches and Breakdown in Gases.* Butterworths advanced physics series. Butterworths, 1964. ISBN: 9780598450210. URL: https://books.google.de/books?id=2nSCvEq6AFcC.

[11] 'The gas electron multiplier (GEM): Operating principlesand applications'. In: *Nuclear Instruments and Methods in Physics Research Section A: Accelerators, Spectrometers, Detectors and Associated Equipment* (7th Aug. 2015). DOI: https://doi.org/10.1016/J.NIMA.2015.07.060.

[12] Bernhard Flierl. 'Particle tracking with micro-pattern gaseous detectors'. PhD. Ludwig-Maximilians-Universität München, 2018.

[13] Katrin Penski. 'Neutral particle detection by a structured cathode of a micro-pattern gaseous detector'. MA thesis. Ludwig-Maximilians-Universität München, 13th Sept. 2020.

[14] RD51. *What is SRS - RD51 scalable readout system.* 11th Aug. 2010. URL: https://indico.cern.ch/event/77597/contributions/2088463/attachments/1056845/1506857/RD51-SRS-Description.pdf (visited on 01/09/2023).

[15] M J French et al. 'Design and results from the APV25, a deep sub-micron CMOS front-end chip for the CMS tracker'. In: *Nucl. Instrum. Methods Phys. Res., A* 466 (2001), pp. 359–65. DOI: 10.1016/S0168-9002(01)00589-7. URL: https://cds.cern.ch/record/516812.

[16] Marcin Byszewski. *Micromegas DAQ system mmDAQ*. 14th Apr. 2011. URL: https://indico.cern.ch/event/132080/contributions/1356987/attachments/98068/139968/byszewski_rd51mtng_mamma_daq.pdf (visited on 01/09/2023).

[17] *ROOT Reference Documentation*. URL: https://root.cern/doc/master/index.html (visited on 01/09/2023).

[18] Katrin Penski. Internal Comunication.

[19] G.Weber. *X-Ray attenuation & absorption calculator*. URL: https://web-docs.gsi.de/~stoe_exp/web_programs/x_ray_absorption/index.php (visited on 01/09/2023).

[20] S. Agostinelli et al. 'Geant4—a simulation toolkit'. In: *Nuclear Instruments and Methods in Physics Research Section A: Accelerators, Spectrometers, Detectors and Associated Equipment* 506.3 (2003), pp. 250–303. ISSN: 0168-9002. DOI: https://doi.org/10.1016/S0168-9002(03)01368-8. URL: https://www.sciencedirect.com/science/article/pii/S0168900203013688.

[21] ANSYS Inc. *ANSYS Mechanical APDL Structural Analysis Guide*. URL: https://www.pdfdrive.com/ansys-mechanical-apdl-structural-analysis-guidepdf-e12262220.html (visited on 01/09/2023).

[22] Rob Veenhof. 'Garfield, recent developments'. In: *Nuclear Instruments and Methods in Physics Research Section A: Accelerators, Spectrometers, Detectors and Associated Equipment* 419.2 (1998), pp. 726–730. ISSN: 0168-9002. DOI: https://doi.org/10.1016/S0168-9002(98)00851-1. URL: https://www.sciencedirect.com/science/article/pii/S0168900298008511.

[23] Rob Veenhof. *Magboltz - transport of electrons in gas mixtures*. URL: https://magboltz.web.cern.ch/magboltz/ (visited on 01/09/2023).

[24] A. Thompson et al. *X-RAY DATA BOOKLET*. 2001. URL: https://xdb.lbl.gov/xdb.pdf.

[25] NIST. *ESTAR : Stopping Power and Range Tables for Electrons*. URL: https://physics.nist.gov/PhysRefData/Star/Text/ESTAR.html (visited on 03/09/2023).

[26] Meteorologisches Institut der Ludwig-Maximilians-Universität München. URL: https://www.meteo.physik.uni-muenchen.de/request-beta/ (visited on 27/07/2023).

[27] Max Herrmann. 'SM2 Micromegas Modules in the Cosmic Ray Facility'. In: Muon Week. 20th Oct. 2020. URL: https://www.etp.physik.uni-muenchen.de/publications/talks/index.html (visited on 02/08/2023).

Appendix A

Support structure technical drawings

All structure seen here are printed by a 3D-printer with PLA (Polyamide) as printing material.

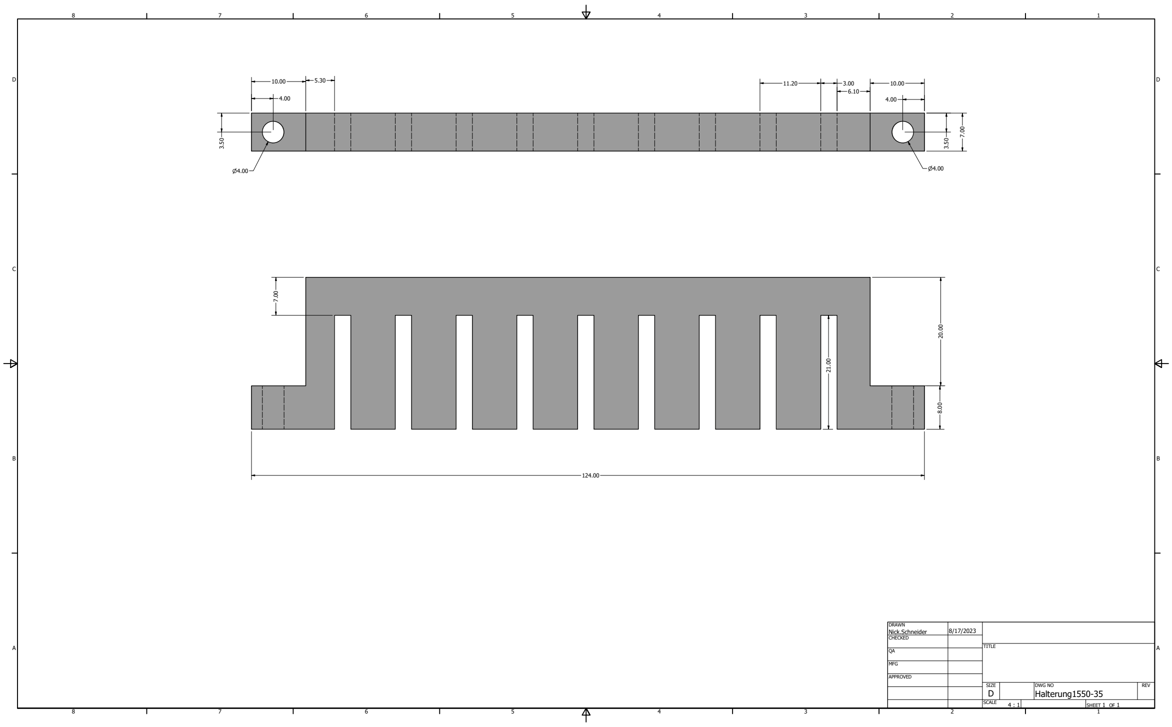

Figure A.1: Main support structure holding converter layers in place. Multiple structures with different slit sizes accommodated to the different layers are used. The slit mid points and distance are the same with the first distance from the right side to the slit mid point is always at 7.6 mm. The holes are not threaded.

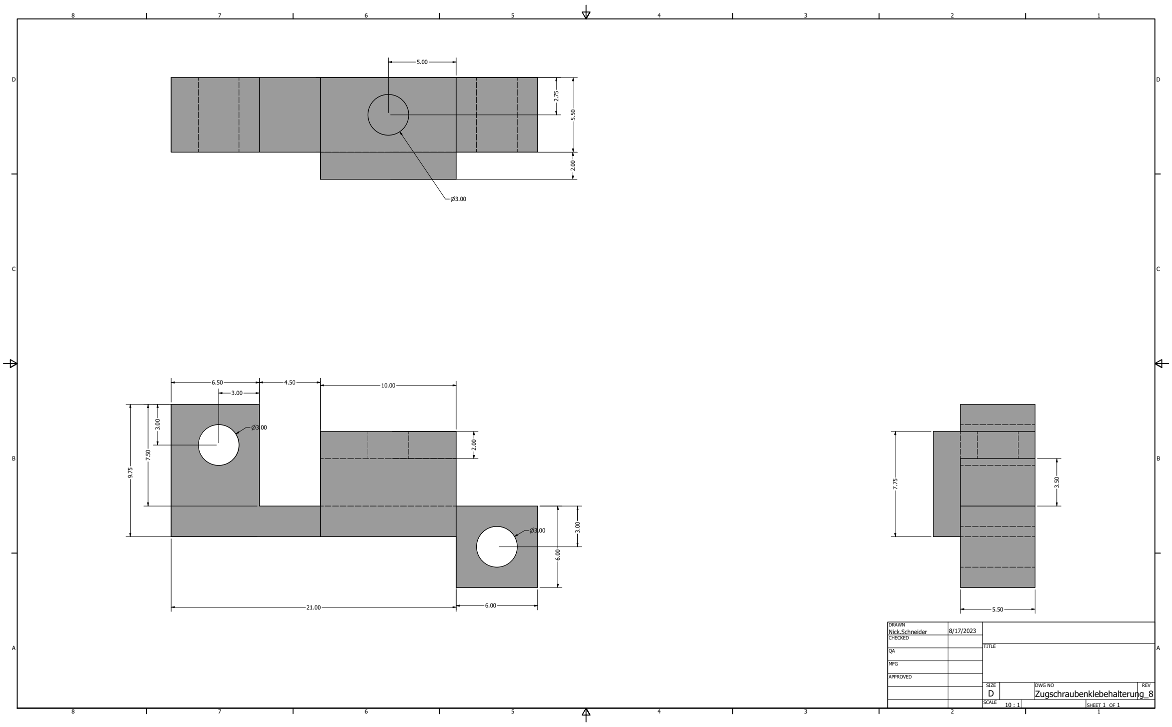

Figure A.2: Structure to apply stress to the converter layers. **Note**: The two holes facing upwards additionally get a M3 thread drilled into them and the singular hole at the front gets a M4 thread although begin given with a diameter of 3 mm. This is needed due to manufacturing inaccuracies of the 3D-printer.

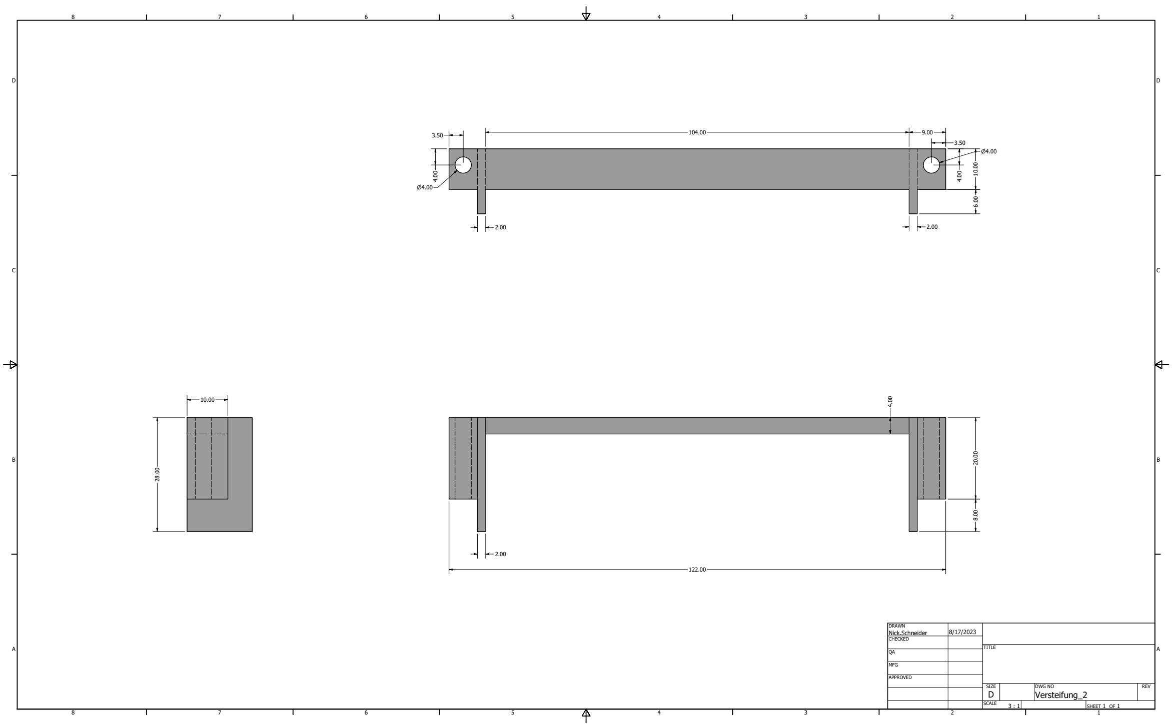

Figure A.3: Structure to prevent tilting of the main structure shown in figure A.1. They fit perfectly in between the main structures and compensate the stresses. The holes are not threaded.

Selbständigkeitserklärung

Ich versichere hiermit, die vorliegende Arbeit mit dem Titel

Effizienzerhöhung für Photonendetektion von mikrostrukturierten Gasdetektoren mittels Materialoptimierung von Konversionsschichten

selbständig verfasst zu haben und keine anderen als die angegebenen Quellen und Hilfsmittel verwendet zu haben.

Nick Andreas Schneider

München, den 13. September 2023